Supercritical Hydrothermal Synthesis of Spinel-Type Non-stoichiometric Cobalt Gallate Nanoparticles and Their Magnetic Properties

Bo Xie[a], *Chiya Numako*[b], *Takashi Naka*[c], *Seiichi Takami*[a*]

[a]Department of Materials Process Engineering, Graduate School of Engineering, Nagoya University, Furo-cho, Chikusa-ku, Nagoya 464-8603, Japan

[b]Department of Chemistry, Graduate School of Science, Chiba University, 1-33 Yayoi-cho, Inage-ku, Chiba 263-8522, Japan

[c]National Institute for Materials Science (NIMS), 1-2-1 Sengen, Tsukuba, Ibaraki 305-0047, Japan

ABSTRACT: The spinel-type metal oxide nanoparticles are known to exhibit various properties, which can be further enhanced by the synthesis of non-stoichiometric nanoparticles. In this work, we report the production of non-stoichiometric cobalt gallate nanoparticles (Co–Ga NPs) with larger inversion parameter that resulted in enhanced magnetic properties compared to previous studies. The synthesis of non-stoichiometric nanoparticles was realized by supercritical hydrothermal process, and without performing the calcination at higher temperature which tended to synthesize thermodynamically stable stoichiometric products. We synthesized Co–Ga NPs with controllable Co/Ga molar ratio, morphology, and particle size at different pH values of the precursor solution. By applying Rietveld refinement, non-stoichiometric Co–Ga NPs were found to have more Co^{2+} occupying tetrahedral and octahedral sites compared to $CoGa_2O_4$, and their superparamagnetic behavior with enhanced spontaneous magnetization at room temperature owing to enhanced and percolated J_{AA}, J_{BB}, and J_{AB} interactions was observed for the first time. We also proposed a possible formation mechanism of non-stoichiometric Co–Ga NPs from cobalt gallium nitrate layered double hydrates in the precursor solutions.

1. INTRODUCTION

Mixed metal oxides with a spinel-type crystal structure have attracted considerable interest owing to their remarkable electrical, optical, magnetic, and catalytic properties.[1] Those properties can be widely applied in fields including but not limited to electrocatalysts,[2-4] gas sensors,[5-7] electrodes of Li- or Mg-ion rechargeable batteries,[8, 9] and photocatalysts.[10, 11] In gas sensor applications, spinel-type $ZnFe_2O_4$ exhibits high sensitivity, selectivity, and fast response to Cl_2 gas owing to its n-type semiconductor behavior.[5] Since tetrahedral and octahedral sites within the spinel-type crystal structure can accommodate metal ions with different ionic radii, spinel-type $ZnCo_2O_4$ can maintain a stable crystal structure during the extraction and insertion of Mg^{2+} as a cathode material in Mg-ion rechargeable batteries with improved cyclability.[9] Meanwhile, manifold compositions of spinel compounds can enable the use of compounds like $FeCo_2O_4$ and $CoFe_2O_4$, in energy storage and conversion systems, since transition metal oxides can hold several oxidation states that favor rapid redox reactions.[12] The manipulation of the spinel-type crystal structure such as the implementation of rare-earth metal atoms or oxygen vacancies also allows spinel-type metal oxides to be used as persistent luminescence phosphors and for carbon dioxide decomposition.[13-15]

The diverse properties of spinel-type metal oxides arise from the combination of divalent and trivalent metal elements, represented by A and B in the empirical formula AB_2O_4, respectively. Spinel-type metal oxides can further be divided into normal spinel ($^{IV}(A)^{VI}[B_2]O_4$), inverse spinel ($^{IV}(B)^{VI}[AB]O_4$), and partially inverse spinel structures. Moreover, synthesis conditions, heat treatment, or chemical environment can play a crucial role in the distribution of A and B cations, further dictating the properties such as magnetic behavior, catalytic activity, and conductivity.[16, 17]

As a prospective candidate in power devices, Ga_2O_3 is a semiconducting oxide with a wide bandgap of approximately 4.9 eV.[18] It shows polymorphism exhibiting α, β, γ, δ, ε, and a recently reported κ forms.[19, 20] Moreover, owing to its electronic properties, optical properties, as well as significant chemical and thermal stability, it finds applications in catalysts, phosphors, and electroluminescent devices, gas sensors.[21, 22] As one of the previously introduced polymorphs, spinel-type γ-Ga_2O_3 exhibits intrinsic Ga vacancies in both tetrahedral and octahedral sites, as reported by Playford *et al*.[20] Therefore, γ-Ga_2O_3 can be an efficient host accommodating and replacing a transition metal or rare-earth metal element, which can further broaden its application scope. In recent years, spinel-type Ga-based metal oxides such as $FeGa_2O_4$, $CuGa_2O_4$, $CdGa_2O_4$, and $ZnGa_2O_4$ have been studied for use as magnetic materials, gas sensors, photocatalysts, and transparent conductors.[23-27] As a spinel-type Ga-based metal oxide, $CoGa_2O_4$ has been considered for applications in ceramic pigments, p-type conductors,[28] gas sensors,[29] electrocatalysts,[30, 31] and cathodes and anodes for various types of capacitors[32-35] owing to its superior conductivity, electrochemical activity, and energy storage capability. It has a partially inverse structure, as shown in Figure 1, where divalent and trivalent cations, i.e., Co^{2+} and Ga^{3+} occupy both tetrahedral and octahedral sites. The empirical formula of $CoGa_2O_4$ is $^{IV}(Co_{1-x}Ga_x)^{VI}[Co_xGa_{2-x}]O_4$, where x represents the degree of inversion showing the fraction of divalent cations in the octahedral site.

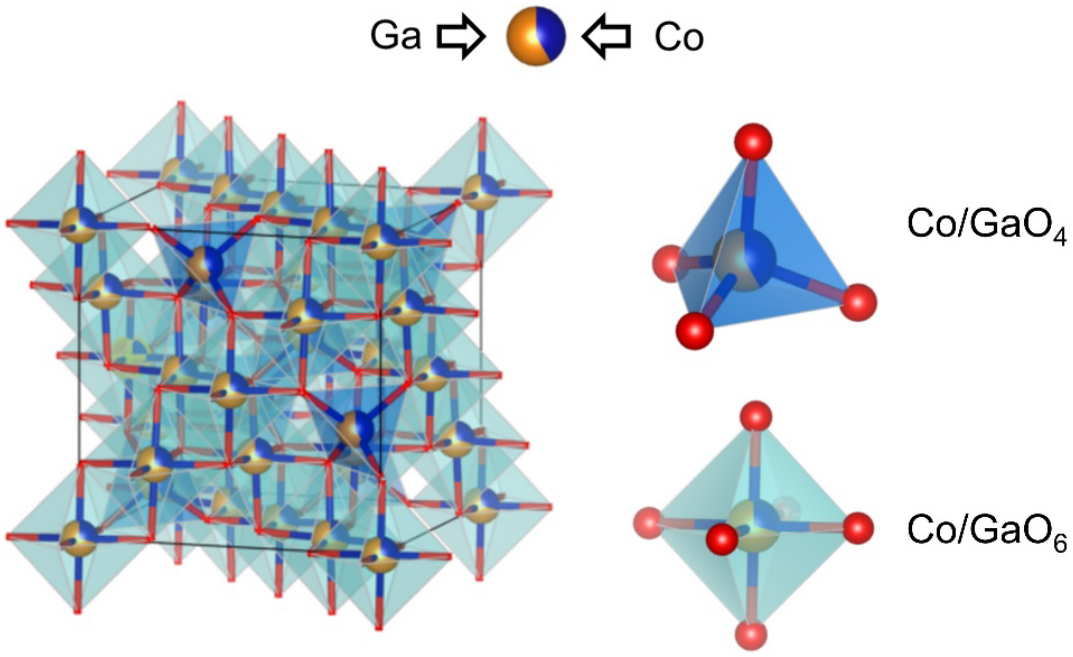

Figure 1. Crystal structure of a partially inverse $CoGa_2O_4$ created by VESTA.[36]

There are newly emerged demands of producing non-stoichiometric spinel-type metal oxides with nanosize for the purpose of improved properties. Actually, photocatalytic properties of spinel compounds were improved by decreasing particle size,[37] and nanosizing affected the magnetic and dielectric properties of materials used in gas sensing.[38] In addition, non-stoichiometric spinel compounds also possess the potential for exhibiting different properties that have not been seen in their stoichiometric counterpart. For example, Gokul *et al*. produced non-stoichiometric cobalt ferrite oxides and discovered field-dependent magnetizations that are different to either $CoFe_2O_4$ or Fe_3O_4 at 300 K.[39]

For the production of $CoGa_2O_4$, traditional synthesis methods usually require a precursor produced from electrodeposition,[32] chemical vapor deposition,[40] electrospinning,[29] or simple hydrothermal or solvothermal treatment,[31, 34, 35, 41] followed by calcination conducted at 600–

1000 °C for several hours. Such calcination process favors the production of thermodynamically stable phase of $CoGa_2O_4$, however, it may cause the agglomeration of products. For the synthesis without the application of the calcination process, Playford *et al*. employed the solvothermal method at a synthesis temperature of 240 °C for six days by making use of a mixture containing metallic gallium and cobalt nitrate hexahydrate and successfully produced stoichiometric $CoGa_2O_4$ with high crystallinity and a size range of 20–40 nm.[17] However, trials on the production of non-stoichiometric spinel-type cobalt gallate nanoparticles (Co–Ga NPs) and studies on their properties have been rarely studied.

In this work, we report the supercritical hydrothermal synthesis of Co–Ga NPs at 400 °C for 10 min without performing the calcination process. Contrary to previous studies, which either calcinated a hydrothermally or solvothermally prepared precursor[31, 34, 35, 41] or treated the precursor in a solvothermal environment for a long time,[17] we produced Co–Ga NPs using a short synthesis time without performing calcination. As a result, spinel-type non-stoichiometric Co–Ga NPs with a broad range of Co/Ga molar ratios were hydrothermally synthesized using supercritical water by controlling the pH value of the precursor solution. Owing to different Co^{2+} occupancies within tetrahedral and octahedral sites in those non-stoichiometric Co–Ga NPs compared to $CoGa_2O_4$, enhanced magnetic behavior at room temperature was observed. In addition, we also propose a possible formation mechanism of non-stoichiometric Co–Ga NPs produced by present technique.

2. EXPERIMENTAL SECTION

2.1. Materials. Cobalt (II) nitrate hexahydrate ($Co(NO_3)_2•6H_2O$, 99.5%), gallium (III) nitrate n-hydrate ($Ga(NO_3)_3•nH_2O$, n = 7–9, 99.9%), nitric acid (HNO_3, weight fraction in the range of 60%–61%), hydrochloric acid (HCl, weight fraction in the range of 35.0%–37.0%), hydrogen peroxide (H_2O_2, 30.0%–35.5%), cobalt (II, III) oxide (Co_3O_4, practical grade), and β-gallium oxides (β-Ga_2O_3, 99.99%) were purchased from FUJIFILM Wako Pure Chemical Co. Sodium hydroxide (NaOH, purity over 97.0%) was purchased from Kishida Chemical Co., Ltd., and they were used as received without further purification.

2.2. Preparation of Co–Ga NPs. The precursor solution was prepared by dissolving cobalt (II) nitrate hexahydrate and gallium (III) nitrate n-hydrate with a concentration of 0.050 mol/L and 0.10 mol/L, respectively (Co/Ga = 0.5) in pure water (2.0 ml). To this aqueous solution (pH around 2–3), 0.56 mL, 0.70 mL, 0.77 mL, and 0.98 mL of 1.0 mol/L NaOH solution was added to adjust pH to 5, 7, 9, and 11. Consequently, the obtained precursor solutions had pale pink precipitates, and the added volume of NaOH was recorded for each condition. The precursor solutions including solid precipitates (1.5 mL) were then transferred to a pressure-resistant Hastelloy reactor (inner volume of 5.0 mL) and put in a furnace whose temperature was maintained at 400 °C in advance. After 10 min, the reactor was taken out and submerged into a cold-water bath at room temperature to terminate the reaction. Solid and liquid products were collected and separated for further analysis.

2.3. Product collection and purification. After performing centrifugation and decantation three times using ion-exchanged water, the solid products were analyzed by scanning electron microscopy (SEM), and the samples of the solid products were freeze-dried (FDS-1000+7E-C, Tokyo Rikakikai Co., Ltd.) for X-ray diffraction (XRD) analysis. Meanwhile, the supernatants of

the liquid products were analyzed by inductively coupled plasma-atomic emission spectroscopy (ICP-AES) analysis.

2.4. XRD analysis. Freeze-dried solid products were put on a silicon sample holder and analyzed by AERIS (PANalytical) with CuKα radiation operating at 40 kV and 15 mA. Diffraction patterns were recorded in the range of $10^{o} < 2\theta < 70^{o}$.

2.5. SEM analysis. The samples were observed by JEOL JSM-7500FA with an accelerating voltage of 15 kV. To evaluate the product size, Feret diameter was measured for at least 400 particles for one synthesis condition. Meanwhile, element composition was investigated by applying energy-dispersive X-ray spectroscopy (EDS).

2.6. ICP-AES analysis. ICP-AES analysis was performed using SPS7800 (Seiko Instruments) to investigate the concentrations of metal elements in the supernatants of the reactant solutions after supercritical hydrothermal synthesis, as well as the aqueous solutions of the precursors. Standard solutions for ICP-AES analysis were purchased from FUJIFILM Wako Chemicals Co. Moreover, ICP-AES analysis was applied to the measurement of the concentrations of various metal elements in the produced solid products. The produced solid products were dissolved in a mixture of nitric acid and hydrogen peroxide with a volume ratio of 1:1. For solid particles which were hard to dissolve, hydrochloric acid was added.

2.7. X-ray absorption fine structure (XAFS) analysis. To evaluate the chemical conditions of Ga and Co in the solid product, Ga K-edge and Co K-edge XAFS spectra were measured with the transmission mode at BL-9A, Photon Factory, KEK, Japan. Every product was mixed with a BN reagent in an agate mortar, made into a disk with 10 mm φ, and put into a polyethylene bag. REX2000[42] software (RIGAKU) was used for the data processing of the X-ray absorption near edge structure (XANES) and extended X-ray absorption fine structure (EXAFS) analyses.

2.8. Rietveld refinement. Rietveld refinement for crystal structure refinement was conducted using RIETAN-FP developed by Izumi et al.[43] The crystal information file of $CoGa_2O_4$ with an ICSD number of 172183 was used and standardized before Rietveld refinement (Table 1). A split pseudo-Voigt function of Toraya was used for a profile function,[44] and the conjugate-direction method was used as the least-squares method. Basic parameters such as shift parameters for profile function and asymmetry parameters, as well as decay parameters, were refined to obtain good fitting, followed by the refinement of atom occupancy. The atom displacement parameter was fixed, and linear constraints were determined based on the Co/Ga molar ratios measured by ICP-AES.

2.9. Magnetic measurements. Alternating current (AC) and direct current (DC) magnetization measurements were conducted using the magnetic properties measurement system (MPMS-XL; Quantum Design). The samples loaded in a gelatin capsule were cast with paraffin to prevent nanoparticle rotation under a magnetic field.

Table 1. Standardized crystal structure of $CoGa_2O_4$

Atom	x	y	z	Site	Occupancy
Co1	0.37500	0.37500	0.37500	8b	0.425
Ga1	0.37500	0.37500	0.37500	8b	0.575
Co2	0.00000	0.00000	0.00000	16c	0.288
Ga2	0.00000	0.00000	0.00000	16c	0.712
O	0.24158	0.24158	0.24158	32e	1.000

3. RESULTS AND DISCUSSION

3.1. Effect of precursor solution pH on composition and Co^{2+} site distribution in Co–Ga NPs.

XRD diffraction patterns of the produced solid particles are shown in Figure 2. Relatively broad diffraction patterns revealed that the particles were nanocrystals. The diffraction patterns for pH 5–11 were indexed based on an ICSD card (ICSD: 172183) of single-phase spinel-type cobalt gallium metal oxides ($CoGa_2O_4$) with a cubic *F d* -3 m space group and were found to shift toward higher angles. In the solid product prepared without NaOH, the peak attributable to the 003 reflection of α-Co $(OH)_2$ reported by Liu *et al*.[45] was labeled with a circle, and peaks attributable to the unidentified contamination were labeled with triangles. Moreover, the reduced full width at half-maximum of the (113) peak indicated an increased crystallite size of the produced Co–Ga NPs as the pH value increased. The average crystallite sizes of the nanocrystals were calculated using Scherrer's equation as summarized in Table 2.

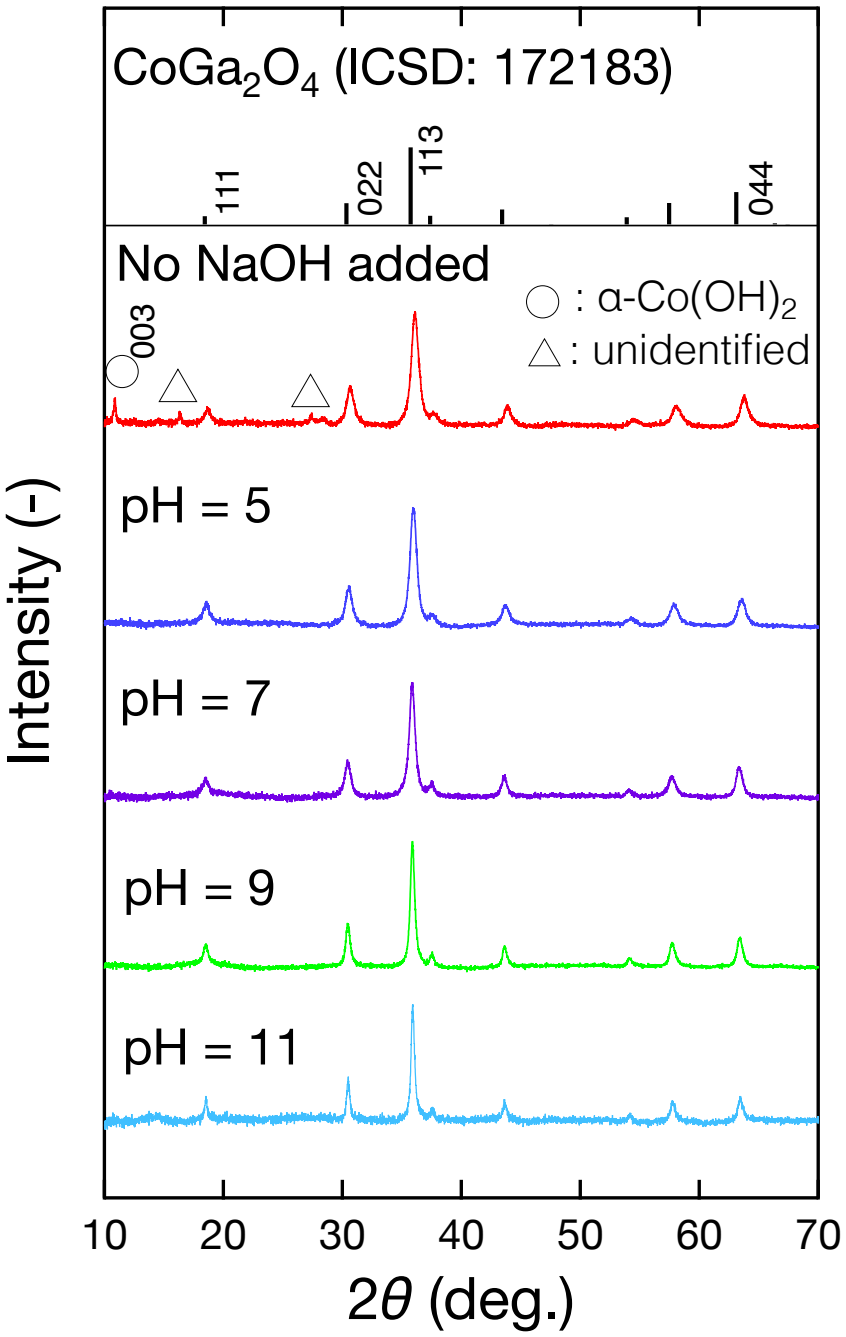

Figure 2. X-ray diffraction patterns of solid products produced at 400 °C under various pH values of precursor solutions.

Table 2. Average crystallite sizes of Co–Ga NPs produced at 400 °C from precursor solutions with various pH values calculated using Scherrer's equation

pH of precursor solutions	Calculated average crystallite size (nm)
No NaOH added	13.1
5	14.2
7	15.0
9	22.8
11	28.5

The morphologies of the Co–Ga NPs were characterized by SEM (Figure 3). In general, spherical particles were observed in low-pH conditions, and an increase in the number of cubic nanoparticles was observed at pH 9 and pH 11. The average particle size was in the range of 19 nm to 58 nm with the increased pH value. A great increase in the average particle size was obtained at pH 11 owing to the decreased supersaturation after substantially adding NaOH. Because $CoGa_2O_4$ nanoparticles agglomerate easily,[41] the average particle sizes measured from SEM images were larger than those calculated from Scherrer's equation.

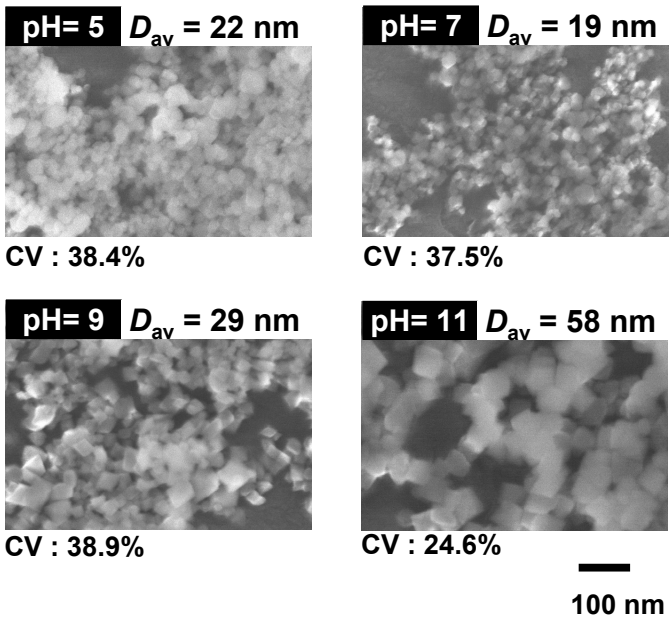

Figure 3. Morphologies and measured average particle sizes of Co–Ga NPs produced at 400 °C under various pH values of precursor solutions (D_{av}: average particle diameter, CV: coefficient of variation).

Before the exploration of the Co/Ga molar ratios of the prepared Co–Ga NPs using ICP-AES, EDS analysis was performed. EDS results showed non-negligible amounts of Ni and Cr when no NaOH was added and at pH 5, which were due to the dissolution of metal elements from the reactor. Therefore, we performed ICP-AES measurements for Co and Ga along with Ni, Cr, and Fe. ICP-AES results are shown in Figure 4. The concentrations of Ni and Cr, as well as Fe, decreased significantly to nearly zero with the increased pH, indicating that higher pH values, i.e., pH 7, pH 9, and pH 11 are suitable for the synthesis of Co–Ga NPs with nearly no contamination. Figure 4 also shows Co/Ga molar ratios. At high pH conditions, the Co/Ga molar ratios of the produced Co–Ga NPs exceeded the stoichiometric composition of Co/Ga = 0.5.

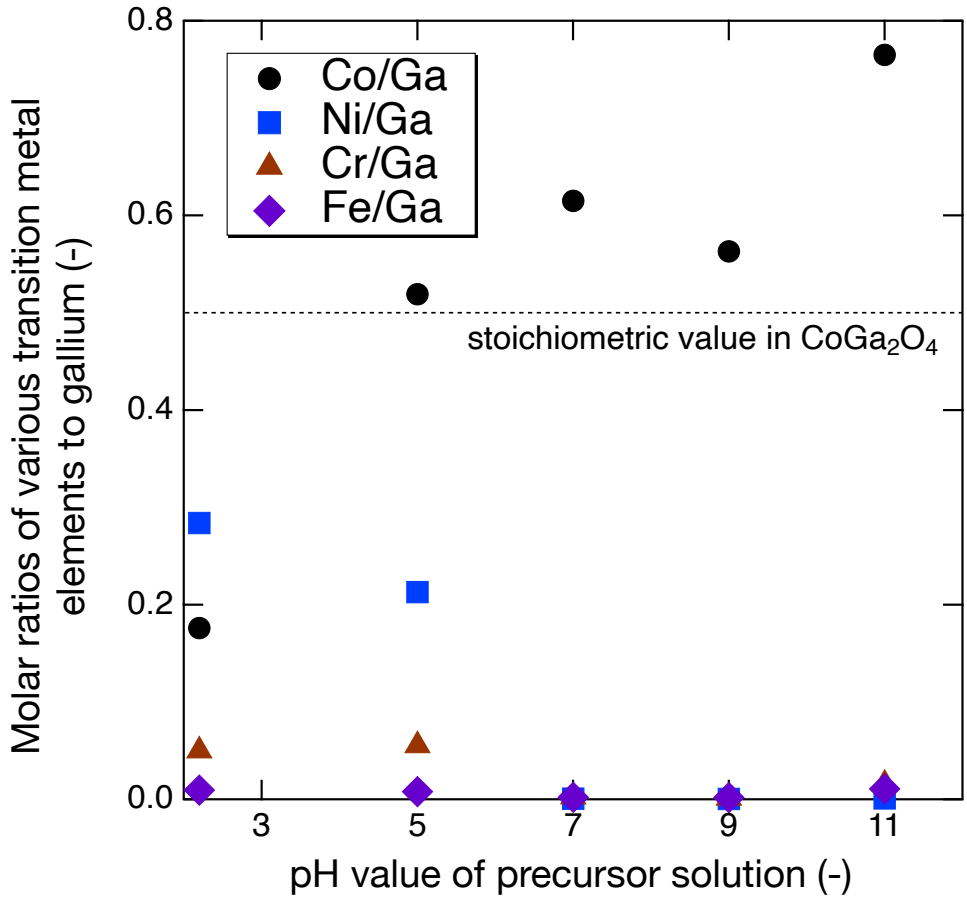

Figure 4. M/Ga (M = Co, Ni, Cr, and Fe) molar ratios of Co–Ga NPs produced at 400 °C under various pH values of precursor solutions measured by ICP-AES.

Because there are more cobalt atoms in the prepared non-stoichiometric Co–Ga NPs compared to $CoGa_2O_4$, Rietveld refinement using RIETAN-FP[43] was applied to investigate the detailed site distribution of metal atoms. First, Ga and Co K-edge XANES analyses were performed to evaluate the valance states of prepared Co–Ga NPs in comparison to purchased references and spinel-type $CoGa_2O_4$ calcinated at 1300 °C for 24 hours by the solid-state reaction method using mixed powders of CoO and Ga_2O_3. Then, the compositions of the prepared Co–Ga NPs were calculated based on the ICP-AES and valance results. Figure 5 shows the obtained spectra. The results confirmed that Co^{2+} and Ga^{3+} were the main valances for the NPs produced at pH 7–11.

However, the peaks greatly shifted to the right for the NPs produced at pH 5, which could indicate a large portion of Co^{3+} ions. Therefore, Rietveld refinements were not conducted for pH 5 because of the contamination issues and the complicated valance states, and "No NaOH added" for the reason of a secondary crystalline phase. Meanwhile, the number of the oxygen atom was fixed at 4 in the final given composition while keeping charge neutrality. Moreover, because there is almost no oxygen vacancy within the spinel-type γ-Ga_2O_3,[20] the oxygen vacancy of the produced Co–Ga NPs was not considered. Thus, the total number of metal atoms in a unit cell was considered to be extremely close to 24 during the refinement. An example of the Rietveld refinement of the diffraction pattern of Co–Ga NPs with a composition of $Co_{1.09}Ga_{1.94}O_4$ at pH 9 and 400 °C is presented in Figure 6, and all results of the refinement along with the calculated composition based on the ICP-AES results are listed in Table 3. For each condition, the calculated versus measured diffraction patterns showed good agreement. Surprisingly, the inversion parameters of the produced Co–Ga NPs were relatively higher compared to those reported by Melot *et al.*,[46] Ikeda *et al.*[47] as well as Naka *et al.*,[48] which were 0.630, 0575, and 0.664, respectively.

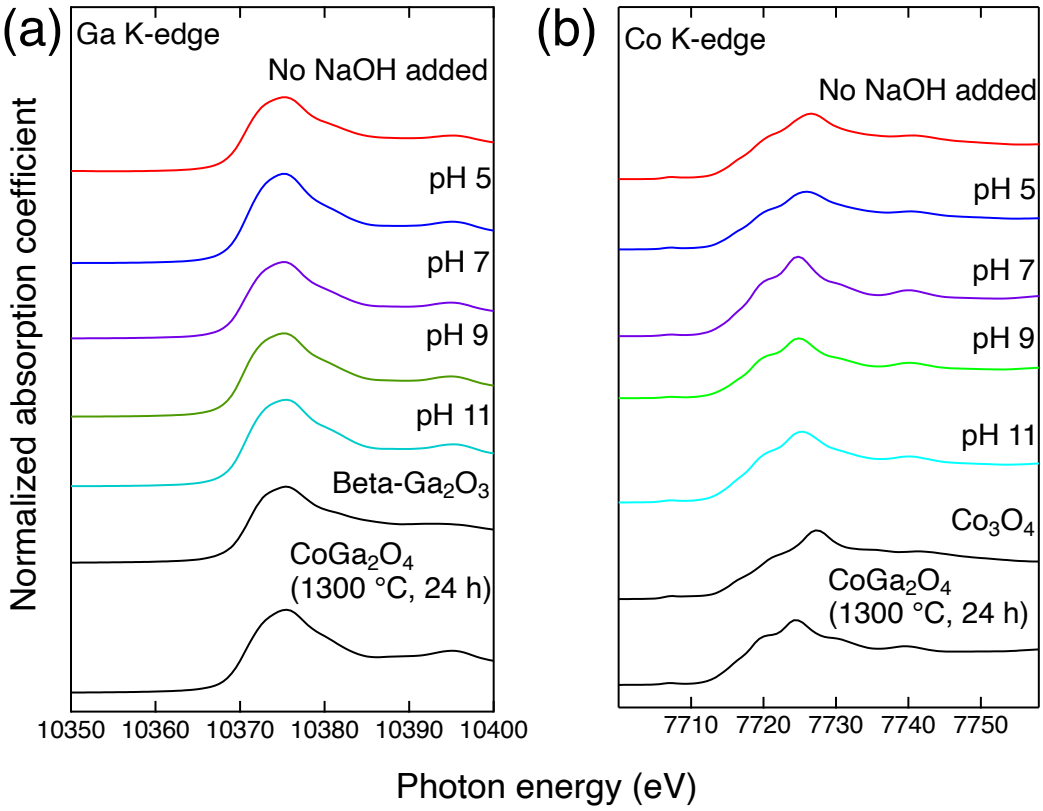

Figure 5. (a) Ga and (b) Co K-edge X-ray absorption near edge structure spectra of non-stoichiometric Co–Ga NPs produced at 400 °C under various pH values of precursor solutions.

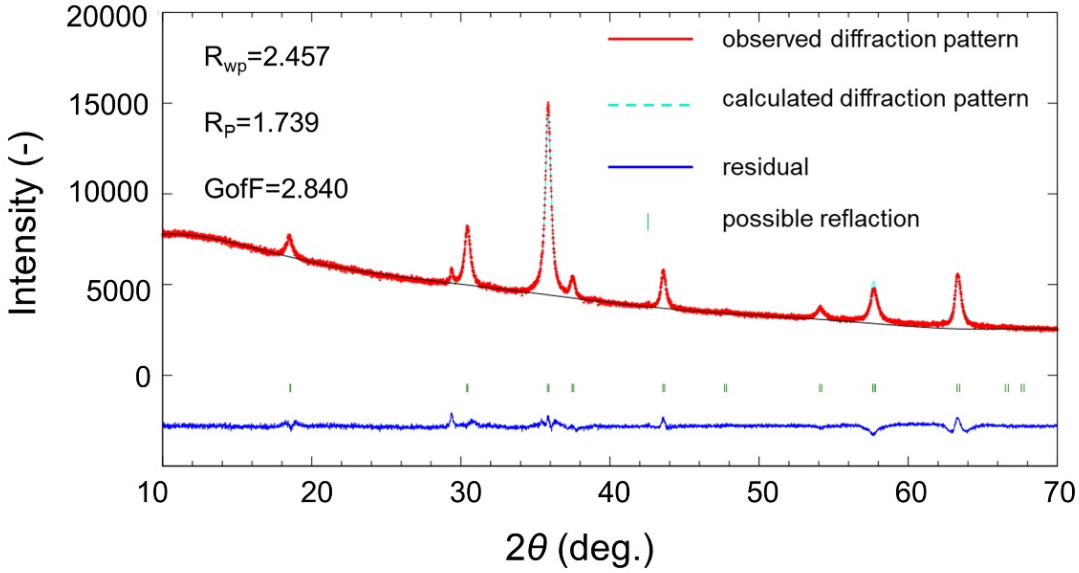

240

241 **Figure 6.** Example (pH 9, 400 °C) of Rietveld refinement using RIETAN-FP in this study.

242

243 **Table 3.** Rietveld refinement results of non-stoichiometric Co–Ga NPs produced at 400 °C using

244 precursor solutions with pH 7–11

Atom	Site	Occupation	Crystal size	Inversion parameter	GOF
pH 11, $Co_{1.35}Ga_{1.77}O_4$					
Co1	8b (Tet.)	0.4299	8.327	0.8676	2.049
Ga1	8b	0.5731			
Co2	16c (Oct.)	0.4338			
Ga2	16c	0.5647			
O	32e	0.9628			
pH 9, $Co_{1.09}Ga_{1.94}O_4$					
Co1	8b	0.5018	8.334	0.5774	2.840
Ga1	8b	0.5308			
Co2	16c	0.2887			
Ga2	16c	0.6946			
O	32e	0.9898			
pH 7, $Co_{1.16}Ga_{1.89}O_4$					
Co1	8b	0.4438	8.331	0.6972	2.196
Ga1	8b	0.5598			
Co2	16c	0.3486			
Ga2	16c	0.6495			
O	32e	0.9823			

The occupancies of Ga and Co calculated from Rietveld refinement in either tetrahedral or octahedral sites of the prepared spinel-type Co–Ga NPs are summarized in Figure 7. The occupancies of Ga atoms in both tetrahedral and octahedral sites at each pH value were lower than those in $CoGa_2O_4$, and the occupancy of Co atoms slightly exceeded that in $CoGa_2O_4$ in tetrahedral sites, and an even more increase was observed in octahedral sites at pH 7 and pH 11.

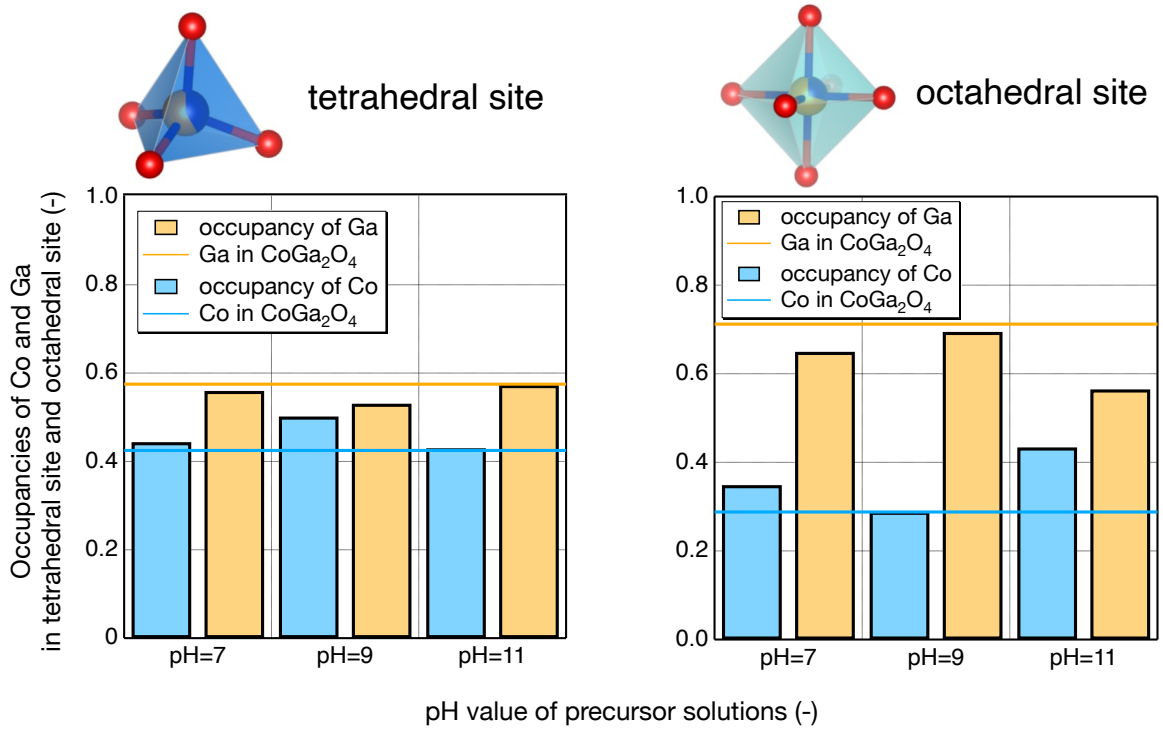

Figure 7. Occupancies of Ga and Co in tetrahedral and octahedral sites derived from Rietveld refinement results of non-stoichiometric Co–Ga NPs produced at 400 °C using precursor solutions with pH 7–11.

The results of the radial structure functions of Ga and Co atoms derived from the EXAFS analysis of Co–Ga NPs prepared at various pH values, as well as $CoGa_2O_4$ produced by the solid-state reaction method are summarized in Figure 8. Prepared non-stoichiometric Co–Ga NPs are showing typical shape of the radial structure function of a spinel compound when compared

with $CoGa_2O_4$. The peak around 1.5 Å is attributable to Ga–O and Co–O interactions, and two intensive peaks ranging from 2.5 to 3.5 Å are attributable to Ga–Ga and Ga–Co interactions (Figure 8 (a)), and Co–Co and Co–Ga interactions (Figure 8 (b)).

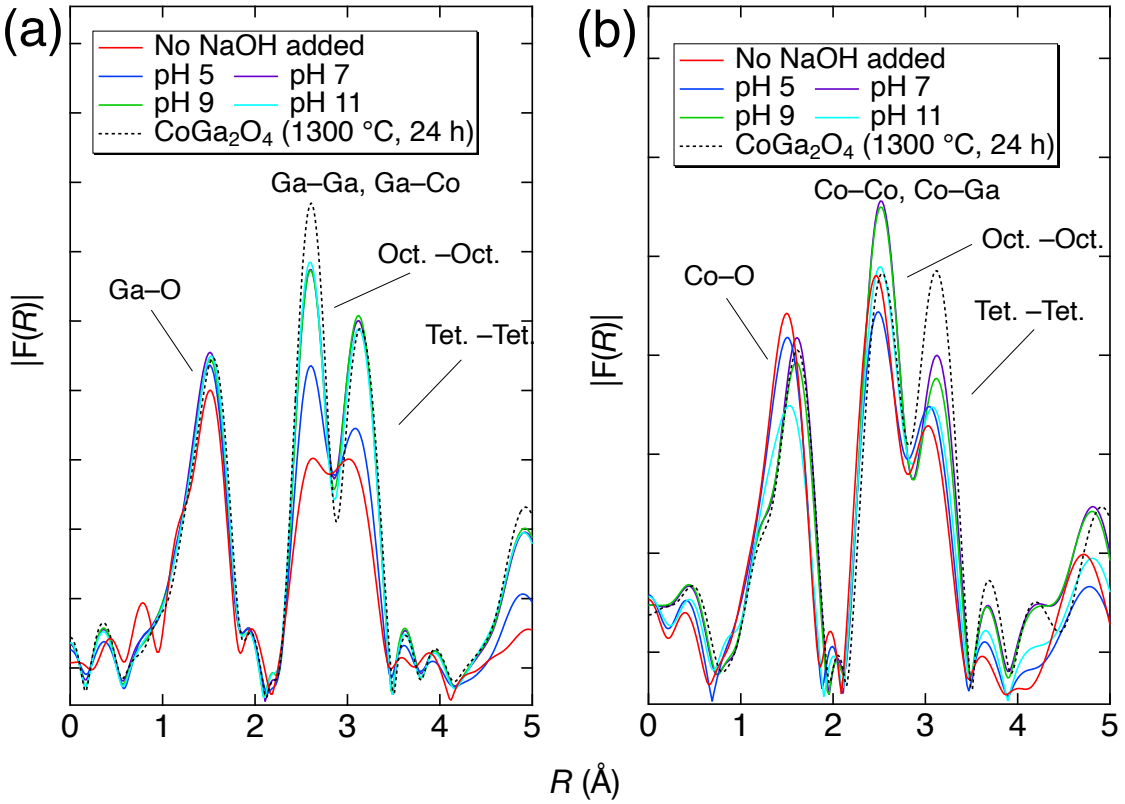

Figure 8. Radial structure function of (a) Ga and (b) Co derived from the extended X-ray absorption fine structure analysis of non-stoichiometric Co–Ga NPs produced at 400 °C under various pH values of precursor solutions.

In Figure 8 (a), regarding the radial structure function of Ga, peaks around 2.5 Å and 3.0 Å refer to Ga–Ga and Ga–Co interactions in octahedral and tetrahedral sites respectively. The shape of the peaks at "No NaOH added" is closer to γ-Ga_2O_3 owing to similar occupancy of Ga in octahedral and tetrahedral sites,[20] and the shape at pH 5 became closer to a spinel compound. Meanwhile, non-stoichiometric Co–Ga NPs prepared at pH 7, 9, and 11 have similar intensities

at tetrahedral site (3.0–3.5 Å) due to comparable degree of crystallinity and Ga occupancy, but lower at octahedral site (2.5–3.0 Å) when compared to $CoGa_2O_4$ due to decreased Ga atoms. In Fig. 8 (b), the radial structure function of Co, the intensities of all three peaks in the range of 1.5–3.5 Å at pH 11 greatly decreased, which might be due to the decreased crystallinity of the local environment around Co atoms in a non-stoichiometric spinel compound.

In summary, spinel-type non-stoichiometric Co–Ga NPs with the Co/Ga molar ratio larger than 0.5 were successfully prepared at pH 7–11. They were found to hold more cobalt atoms within the octahedral site, but lower crystallinity when compared to $CoGa_2O_4$.

3.2. Magnetic properties of the produced non-stoichiometric Co–Ga NPs.

Since cobalt ions is the only magnetic ion, their site distribution could affect super-exchange interactions between Co^{2+} ions, that is, tetrahedral–tetrahedral exchange interaction J_{AA}, octahedral–octahedral exchange interaction J_{BB}, and tetrahedral–octahedral exchange interaction J_{AB}. Therefore, non-stoichiometric Co–Ga NPs with more Co^{2+} within the octahedral site prepared by present technique might exhibit different magnetic behavior compared to $CoGa_2O_4$. Regarding the magnetic behavior of $CoGa_2O_4$, density functional calculations conducted by Rafiq *et al*. revealed the ferromagnetic behavior of spinel-type $CoGa_2O_4$, assuming that Co ions completely occupy the tetrahedral sites.[49] However, in the Co–Ga NPs produced in this work, Co^{2+} occupied both tetrahedral and octahedral sites. Fiorani *et al*.[50] revealed an antiferromagnetic order of $CoGa_2O_4$ with T_N = 10 K, produced from the solid-state reaction method. Similarly, Mathur *et al*.[40] investigated the magnetic properties of $CoGa_2O_4$ NPs produced from the sol–gel method, and the *M–H* curve measured at room temperature showed a typical paramagnetic behavior, i.e., no spontaneous magnetization corresponding with an intercept on the Y axis (see

our results in Figure 9). In our work, compared to $CoGa_2O_4$, the occupancies of the magnetic Co^{2+} ion in tetrahedral (0.443(8), 0.501(8), 0.429(9)) and octahedral (0.348(6), 0.288(7), 0.433(8)) sites of the non-stoichiometric Co–Ga NPs produced at pH 7, 9 and 11 were closer to or even higher than the corresponding percolation thresholds, which were reported to be 0.429(3), 0.390(3), and 0.227(3) for J_{AA}, J_{BB}, and J_{AB}, respectively.[51] Therefore, J_{AA}, J_{BB}, and J_{AB} interactions are considered to be enhanced and percolate through the crystal structures of the products in this work.

The *M–H* curves of the Co–Ga NPs measured at room temperature are shown in Figure 9. Notably, a closed hysteresis loop was obtained, and the magnetic behavior was considered to be the combination of partially paramagnetic and partially ferromagnetic (superparamagnetic) behaviors. In fact, as can be seen in Figure 9, M_g did not saturate at high fields as expected for ferromagnets, and it increased linearly with respect to H. The latter is a typical feature observed in paramagnets. At all pH conditions, Co–Ga NPs with higher Co/Ga molar ratios exhibited larger spontaneous magnetization M_0 (intercepts at $H = 0$ of the extrapolated line from the linear part of $M_g(H)$ curve in Figure 9). Since J_{AA}, J_{BB}, and J_{AB} interactions are enhanced and percolated through the nanocrystal, a magnetic domain develops macroscopically in the crystals as a result. Notably, Co–Ga NPs prepared at pH 11, which had the highest Co/Ga ratio and Co occupancies in tetrahedral and octahedral sites, exhibited the largest spontaneous magnetization at room temperature. For Co–Ga NPs prepared at "No NaOH added" and pH 5 with relatively smaller Co/Ga molar ratios, M_0 is comparable with those for others. Plausibly, the magnetic contaminations Ni and Cr are situated in the cation sites in the spinel structure and contribute to the formation of magnetic domains. In summary, we speculate that the observed ferromagnetism at room temperature is induced by a cationic configurational deviation from that of a normal

spinel[52] and the effects of crystal morphology such as large surface-to-volume ratio, surface anisotropy,[53] and valence transition observed with reduced crystal size in metal oxides could also be considered.[54]

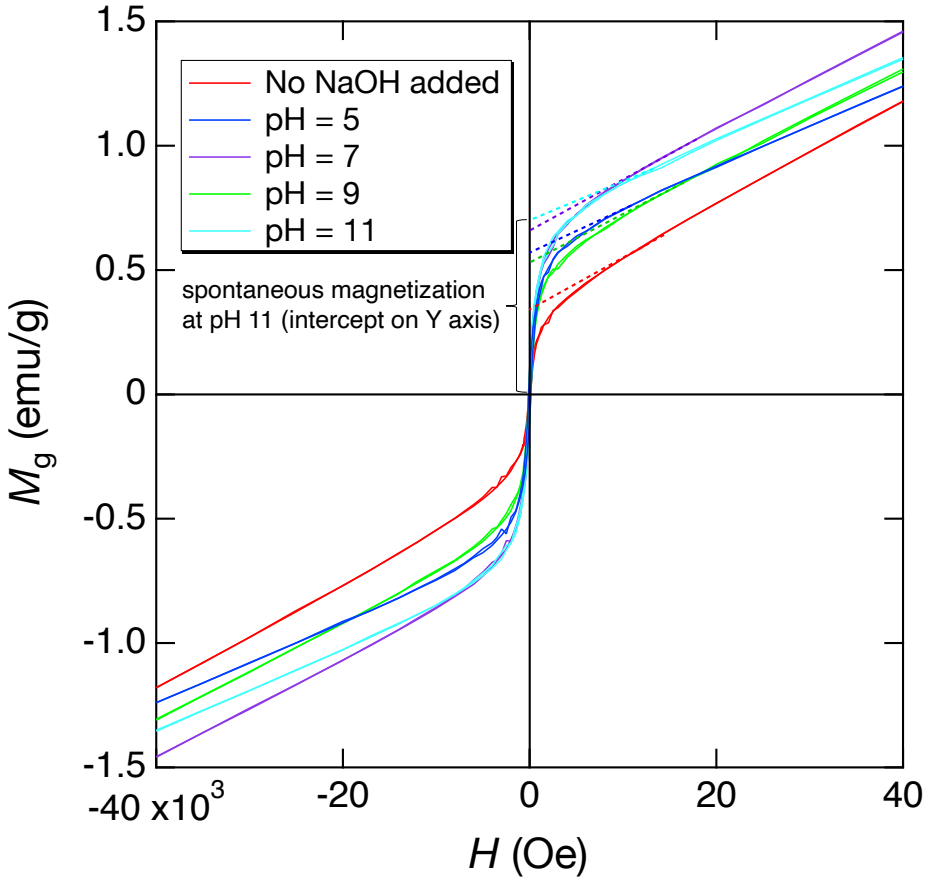

Figure 9. *M–H* curves (measured at room temperature, 300 K) of non-stoichiometric Co–Ga NPs produced at 400 °C under various pH values of precursor solutions.

To further investigate the magnetic properties of our products, *M–T* curves measured at 20 kOe and 50 kOe are summarized in Figure 10 (a) and (b). Based on Eq. 1, which was established for *H* above 15 kOe, both susceptibility χ and M_0 were calculated as a function of temperature (from 2 K to 300 K), as depicted in Figure 10 (c) and (d). Herein, χ is a differential susceptibility defined as $\chi(T) = [M_g(50\ \text{kOe}) - M_g(20\ \text{kOe})]/(50\ \text{kOe} - 20\ \text{kOe})$.

$$M(H) = M_0 + \chi(H)H \quad \text{(Eq.1)}$$

From Figure 10 (c), $\chi(T)$ curves exhibit anomalous cusp and kink below 50 K, which are expected to occur at magnetic transitions. To identify magnetic transitions, we measured AC and DC susceptibilities under small magnetic fields. As a result, a spin-glass phase transition was indicated at spin-glass phase transition temperature (T_{SG}) below 10 K at every pH condition, along with ferri- or ferromagnetic transitions temperature (T_m) below 50 K at "No NaOH added" and pH 5 exclusively. Moreover, in the AC susceptibility, a frequency-dependent peak was found to shift to high temperature with higher frequency. In addition, a cusp at T_{SG} in DC susceptibility measured after zero-field cooling (ZFC) was also observed for each pH condition (see supporting information Figures S1 and S2). Those are typical in spin-glass transition, and transition temperatures were summarized (see supporting information Table S1). Figure 10 (d) shows the reciprocal magnetic susceptibility χ^{-1} as a function of temperature, from which deviations from a modified Curie–Weiss law shown as Eq. 2 were observed above 50 K. Herein, C is the Curie constant, and θ is the Curie–Weiss temperature. We experimentally obtained the effective paramagnetic moment p = 3.74 μ_B for pH 9 deduced from the experimental value C = 1.749(5), which is smaller than but comparable to 4.96 μ_B for the stoichiometric bulk sample, while the Curie–Weiss temperature θ = –28.2 K is considerably higher than that of the bulk (–49.9 K).[48]

$$\chi = C/(T - \theta) \quad \text{(Eq. 2)}$$

Figure 10 (d) also shows the enhancement of the Curie–Weiss temperature θ corresponding to the development of interactions between Co^{2+}. This can be attributed to the strengthened interactions between the increased number of Co^{2+} ions in octahedral sites with the neighboring Co^{2+} ions.[48] To summarize, with the help of enhanced and percolated J_{AA}, J_{BB}, and J_{AB}

interactions owing to large number of cobalt atoms within tetrahedral and octahedral sites, superparamagnetic behavior of non-stoichiometric Co–Ga NPs was observed for the first time. Both effective paramagnetic moment and Curie–Weiss temperature were comparable to the stoichiometric bulk sample.

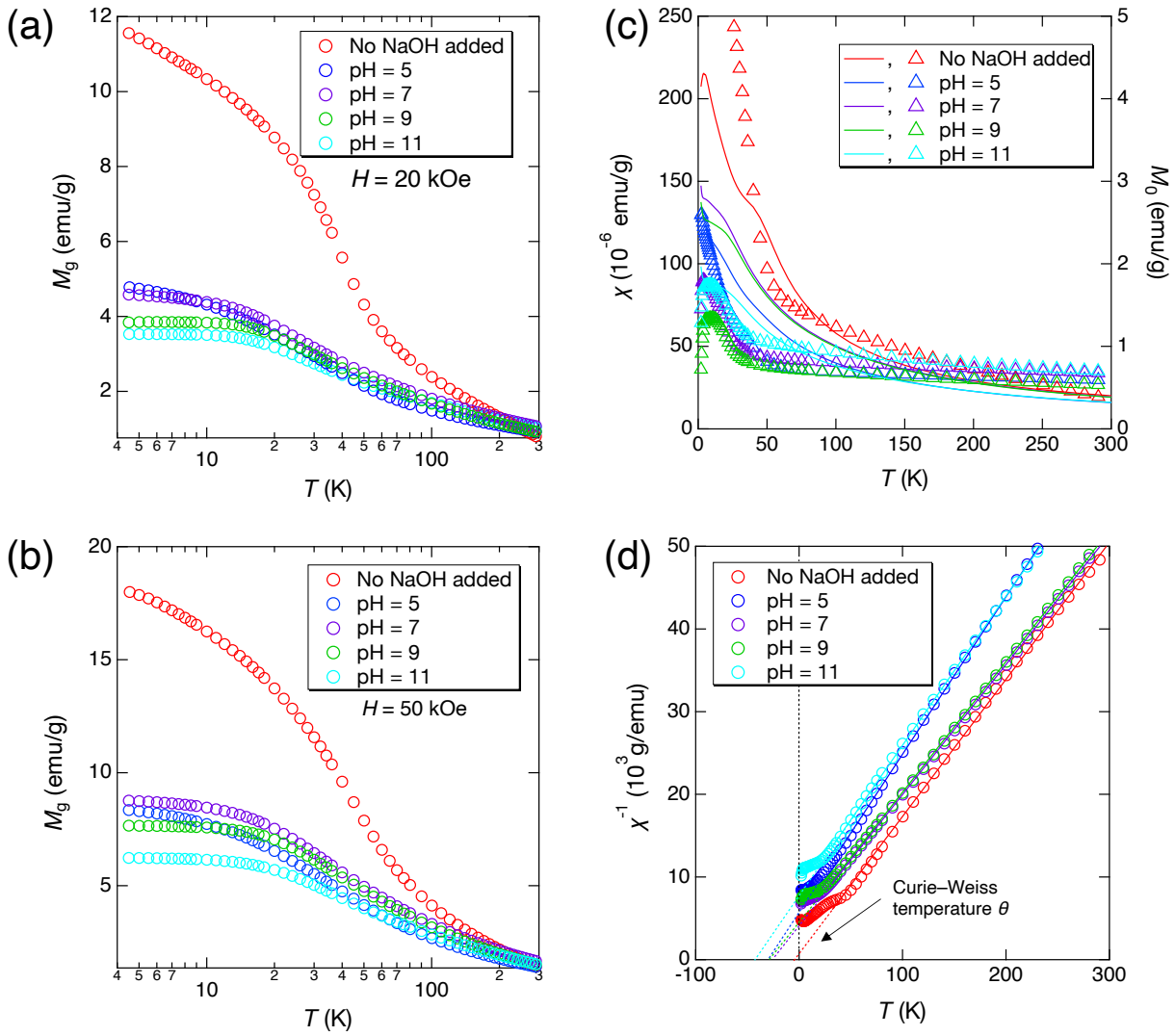

Figure 10. *M*–*T* curves measured at (a) 20 kOe and (b) 50 kOe and (c) χ, m_0 vs T plots and (d) χ^{-1} vs T plots of non-stoichiometric Co–Ga NPs produced at 400 °C under various pH values of precursor solutions.

3.3. Formation mechanism of non-stoichiometric Co–Ga NPs.

To reveal the formation mechanism of non-stoichiometric Co–Ga NPs with high Co/Ga molar ratio, we investigated the crystal phase and the composition (Co/Ga molar ratio) of solid precipitates in the precursor solutions. In addition, solid precipitates were collected on a silicon sample holder for XRD analysis without centrifugation. However, no solid precipitate was observed in the aqueous solution when no NaOH was added. All XRD diffraction patterns of the solid precipitates are shown in Figure 11.

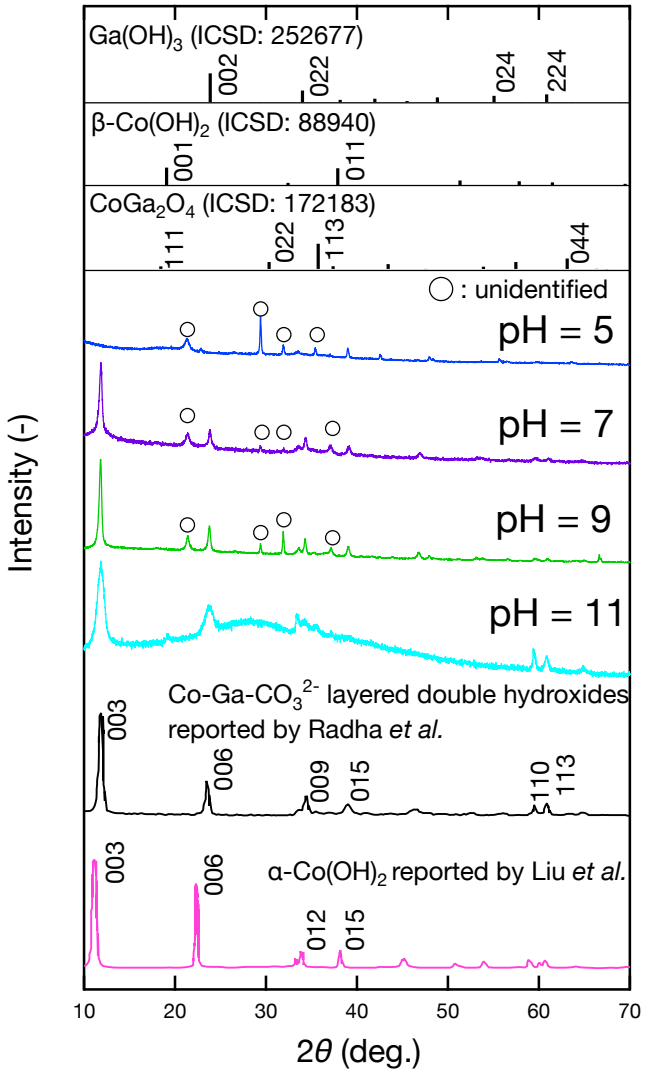

Figure 11. X-ray diffraction (XRD) patterns of solid precipitates in precursor solutions at various pH values. (The XRD patterns of Co–Ga-CO_3^{2-} LDHs and α-Co $(OH)_2$ are plotted based on research papers of Radha *et al*.[55] and Liu *et al*.[45], respectively.)

Comparing with the diffraction pattern of Co–Ga-CO_3^{2-} LDHs reported by Radha *et al*.,[55] we attributed the observed diffraction pattern of the solid precipitate obtained from the precursor solutions at pH 11 to cobalt gallium nitrate layered double hydroxides (Co–Ga-NO_3^- LDHs). Herein, cobalt gallium LDHs consist of positively charged brucite-like layers including interconnected octahedral sites occupied by divalent (M^{2+} = Co^{2+}, Mg^{2+}, and Fe^{2+}) and trivalent (M^{3+}= Ga^{3+}, Al^{3+}, and Fe^{3+}) metal ions, along with interlayer anions (A^{n-} = NO_3^- or CO_3^{2-}) to achieve a neutral environment. A general formula for this type of structure is $[M^{2+}_{1-x}M^{3+}_x(OH)_2]^{x+}[A^{n-}_{x/n}\bullet mH_2O]$, and typically, the molar ratio of $M^{3+}/(M^{3+} + M^{2+})$ was reported to be a value between 0.2 and 0.4 by Wang *et al*.[56] When it comes to the connection between Co–Ga-NO_3^- LDHs and the generation of a spinel-type $CoGa_2O_4$, Cook *et al*. conducted the solvothermal synthesis of spinel-type $CoGa_2O_4$ using gallium metal and cobalt(II) nitrate hexahydrate as starting materials and revealed that the LDH structure can act as a metastable phase, followed by redissolution or amorphization before the final formation of spinel-type $CoGa_2O_4$.[57] Similarly, the diffraction patterns of Co–Ga-NO_3^- LDHs were observed at pH 7 as well as pH 9. The remaining diffraction patterns (labeled by a circle) at pH 5, pH 7, as well as pH 9, were compared with two notable polymorphs of cobalt hydroxide, i.e., β-Co $(OH)_2$ and α-Co $(OH)_2$ reported by Liu *et al*. [45] and gallium hydroxide for further identification. However, they did not match any of those compounds. Therefore, we consider them as an intermediate, which may have disappeared during hydrothermal synthesis.

Then, we conducted ICP-AES analysis to measure the chemical composition in aqueous solution of the precursor solutions at room temperature. Figure 12 shows the detailed molar fractions of Co and Ga (Y axis = 1.0 means no metal element in the solid precipitate). As reported by Hassan Mohamed *et al.*, Co hydrolyzes to $Co(OH)^+$, and consequently, the precipitation of $Co(OH)_2$ initiates when the pH value of the aqueous solution exceeded 7.[58] Similar results were reported by Sheha *et al.* and Dakroury *et al.*[59,60] On the other hand, Ga is an amphoteric metallic element, which dissolves in aqueous solutions at either low or high pH.[61] In our measurements, the proportion of Co (marked as pink circles) in the aqueous solution continuously decreased with an escalating pH value, which is a consequence of the precipitation of Co ions from pH 5 to pH 11. Meanwhile, the proportion of Ga in the aqueous solution (marked as black squares) started to increase from pH 7, which is considered the redissolution process of solid Ga at high pH values.

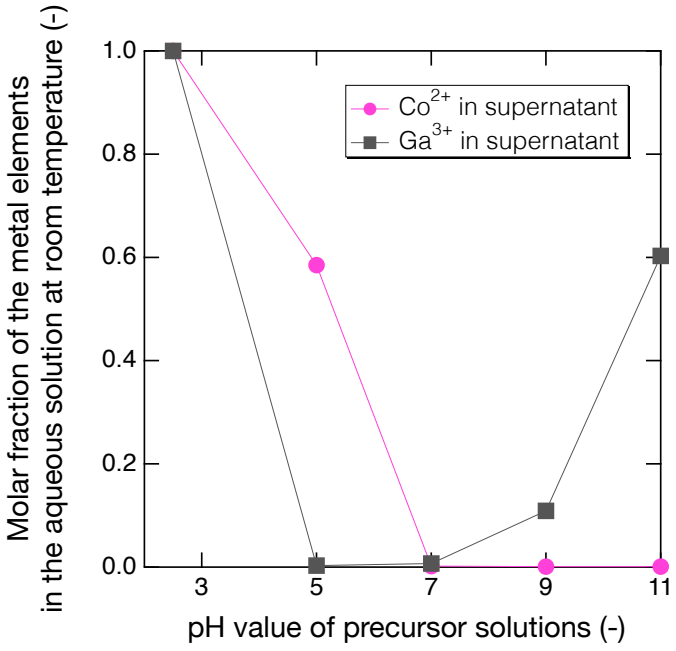

Figure 12. Molar fractions of cobalt and gallium in supernatant of precursor solutions at various pH values.

Next, we evaluated the actual composition (Co/Ga molar ratio) of the solid precipitate in the precursor solution at each condition at room temperature. For a better understanding, the calculation method is shown in Figure 13, where *M* stands for the number of moles, and *C* represents the concentration (mol/L) obtained from ICP-AES analysis.

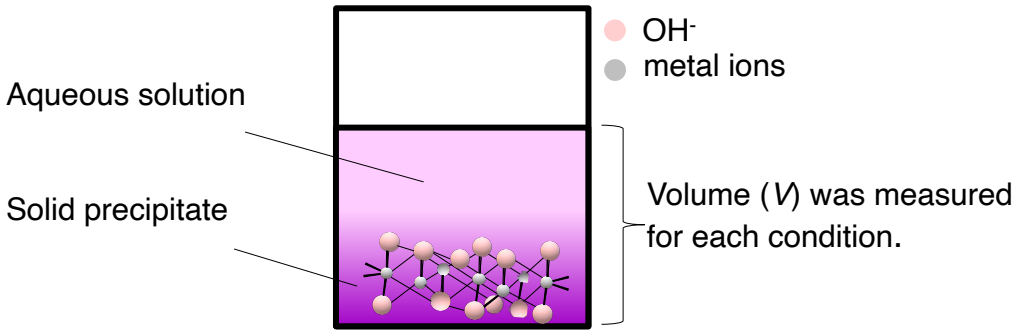

$$M_{(\mathrm{Co,\ precipitate})} = M_{(\mathrm{Co,\ in\ whole\ precursor\ solutions})} - C_{(\mathrm{Co,\ aqusous\ solution})} \times V$$

$$M_{(\mathrm{Ga,\ precipitate})} = M_{(\mathrm{Ga,\ in\ whole\ precursor\ solutions})} - C_{(\mathrm{Ga,\ aqusous\ solution})} \times V$$

Figure 13. Schematic depicting the calculation of chemical composition in the solid precipitate.

Figure 14 shows comparison between calculated Co/Ga molar ratio in the solid precipitate, and that in the final products. The Co/Ga molar ratio of the solid precipitate at room temperature keeps increasing from pH 5 to pH 11 and that of the Co–Ga-NO_3^- LDH obtained at pH 11 was 1.24, which almost resembles the proposed reasonable ratio.[56] Notably, this increasing tendency of Co/Ga molar ratio in the solid precipitate at room temperature is similar to that observed in the final products.

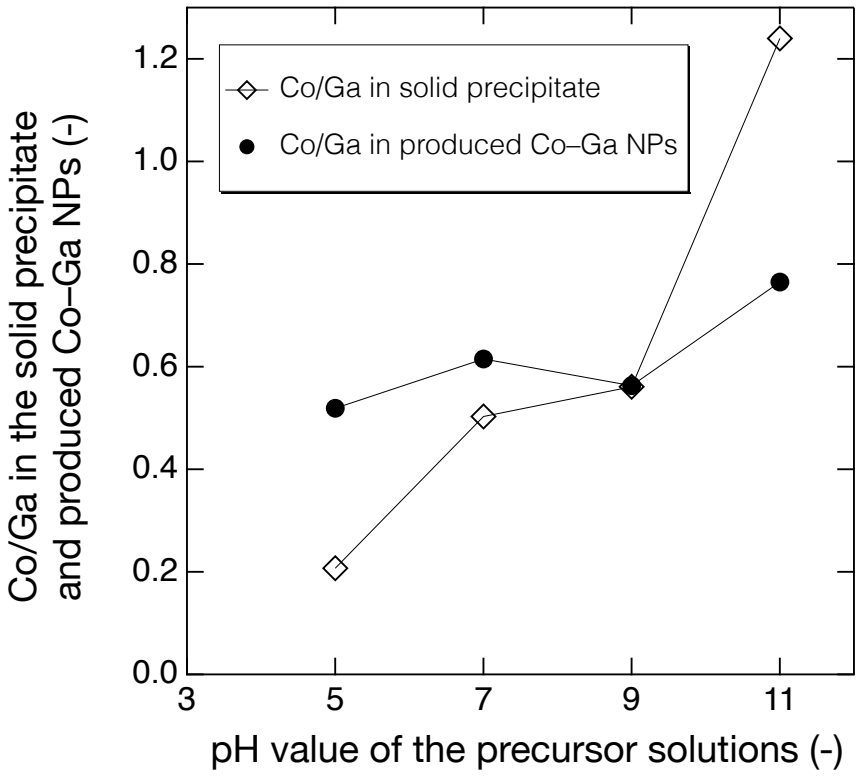

Figure 14. Co/Ga molar ratios in the solid precipitate and produced non-stoichiometric Co–Ga NPs.

Based on the results, we propose a possible formation mechanism in the present technique as follows: The solid precipitate containing Co–Ga-NO_3^- LDHs could form non-stoichiometric Co–Ga NPs during supercritical hydrothermal synthesis in a mechanism similar to that reported by Cook *et al*.[57], while maintaining large Co/Ga molar ratio owing to the absence of calcination at high temperature. However, Co^{2+} and Ga^{3+} in the supernatant of the precursor solutions could react with the solid precipitate during hydrothermal synthesis, especially at pH 5 and pH 11 (See Co^{2+}, Ga^{3+} in supernatant of reactant solutions in supporting information Figures S3). Therefore, the manipulation of the pH value of the precursor solution in the present technique can affect the

solubilities of Co and Ga at room temperature, and further give effect on the Co/Ga molar ratios in the final solid products.

4. CONCLUSIONS

We demonstrated the synthesis of spinel-type non-stoichiometric cobalt gallate nanoparticles (Co–Ga NPs) using fast supercritical hydrothermal synthesis without performing the calcination process. Non-stoichiometric Co–Ga NPs with controllable Co/Ga molar ratios were produced by manipulating the precursor solutions pH. At pH 7 and pH 11, the prepared Co–Ga NPs exhibited large inversion parameters and Co/Ga molar ratios. Produced Co–Ga NPs exhibited a combination of paramagnetic and ferromagnetic (superparamagnetic) behaviors at room temperature, and those prepared at pH 11 with the highest inversion parameter showed the largest spontaneous magnetization M_0 due to percolated J_{AA}, J_{BB}, and J_{AB} interactions. The formation mechanism likely involves solid precipitates containing Co–Ga-$NO3^-$ LDHs or their intermediates in the precursor solutions, which play a key role in the generation of Co–Ga NPs, and we found a tight relationship between Co/Ga molar ratio in the solid precipitate at room temperature and that in the final solid products. Generally, present technique has demonstrated great potentials as effective synthesis method for producing Ga-based spinel-type metal oxides with non-stoichiometric composition that exhibit enhanced properties.

ASSOCIATED CONTENT

Supporting Information

Additional experimental details, including (a) AC susceptibility at various frequencies, DC susceptibility measured after the ZFC of Co–Ga NPs at 400 °C prepared from precursor solutions with pH 5 and 7. (b) Summary of the spin-glass transition temperature T_{sg}, ferri- or ferromagnetic transition temperature T_m, and error of T_{sg} of Co–Ga NPs. (c) Molar fractions of cobalt and gallium in supernatant of reactant solutions after supercritical hydrothermal synthesis at various pH values (PDF).

AUTHOR INFORMATION

Corresponding Author

*Email: takami.seiichi@material.nagoya-u.ac.jp

Author Contribution

Bo Xie : conceptualization, formal analysis, investigation (material production, XRD, SEM, ICP-AES, XAFS measurements), validation, visualization, writing – original draft, writing – review & editing.

Chiya Numako : formal analysis, investigation (XAFS measurements), resources, validation, writing – review & editing.

Takashi Naka : formal analysis, investigation (magnetization measurements), resources, validation, writing – review & editing.

Seiichi Takami : conceptualization, funding acquisition, investigation (XAFS measurements), formal analysis, project administration, resources, supervision, validation, writing – review & editing.

Notes

The authors declare no competing financial interest.

ACKNOWLEDGMENT

This work was supported by JSPS KAKENHI Grant Numbers 17H06467, 20H02514. XAFS measurements were conducted under the approval of the Photon Factory Program Advisory Committee (Proposal No. 2021G143, 2021G584).

REFERENCES

1. Tsurkan, V.; Krug von Nidda, H.-A.; Deisenhofer, J.; Lunkenheimer, P.; Loidl, A. On the complexity of spinels: Magnetic, electronic, and polar ground states. *Phys. Rep.* **2021**, 926, 1–86.

2. Yu, Z.-Y.; Lang, C.-C.; Gao, M.-R.; Chen, Y.; Fu, Q.-Q.; Duan, Y.; Yu, S.-H. Ni–Mo–O nanorod-derived composite catalysts for efficient alkaline water-to-hydrogen conversion via urea electrolysis. *Energy Environ. Sci.* **2018**, 11 (7), 1890–1897.

3. Peng, S.; Gong, F.; Li, L.; Yu, D.; Ji, D.; Zhang, T.; Hu, Z.; Zhang, Z.; Chou, S.; Du, Y.; Ramakrishna, S. Necklace-like Multishelled Hollow Spinel Oxides with Oxygen Vacancies for Efficient Water Electrolysis. *J. Am. Chem. Soc.* **2018**, 140 (42), 13644–13653.

4. Maiyalagan, T.; Jarvis, K. A.; Therese, S.; Ferreira, P. J.; Manthiram, A. Spinel-type lithium cobalt oxide as a bifunctional electrocatalyst for the oxygen evolution and oxygen reduction reactions. *Nat. Commun.* **2014**, 5 (1), 3949.

5. Niu, X.; Du, W.; Du, W. Preparation and gas sensing properties of ZnM_2O_4 (M = Fe, Co, Cr). *Sens. Actuators B Chem.* **2004**, 99 (2-3), 405–409.

6. Mukherjee, K.; Majumder, S. B. Reducing gas sensing behavior of nano-crystalline magnesium–zinc ferrite powders. *Talanta* **2010**, 81 (4-5), 1826–1832.

7. Dilip, R.; Jayaprakash, R. Synthesis and characterization of $BaFe_2O_4$ nano-ferrites for gas sensor applications. *Energ Ecol. Environ.* **2018**, 3 (4), 237–241.

8. Rong, A.; Gao, X. P.; Li, G. R.; Yan, T. Y.; Zhu, H. Y.; Qu, J. Q.; Song, D. Y. Hydrothermal Synthesis of Zn_2SnO_4 as Anode Materials for Li-Ion Battery. *J. Phys. Chem. B* **2006**, 110 (30), 14754–14760.

9. Shimokawa, K.; Atsumi, T.; Harada, M.; Ward, R. E.; Nakayama, M.; Kumagai, Y.; Oba, F.; Okamoto, N. L.; Kanamura, K.; Ichitsubo, T. Zinc-based spinel cathode materials for magnesium rechargeable batteries: toward the reversible spinel–rocksalt transition. *J. Mater. Chem. A* **2019**, 7 (19), 12225–12235.

10. Suresh, R.; Rajendran, S.; Kumar, P. S.; Vo, D.-V. N.; Cornejo-Ponce, L. Recent advancements of spinel ferrite based binary nanocomposite photocatalysts in wastewater treatment. *Chemosphere* **2021**, 274, 129734.

11. Jing, P.; Li, J.; Pan, L.; Wang, J.; Sun, X.; Liu, Q. Efficient photocatalytic degradation of acid fuchsin in aqueous solution using separate porous tetragonal-$CuFe_2O_4$ nanotubes. *J. Hazard. Mater.* **2015**, 284, 163–170.

12. Gao, H.; Liu, S.; Li, Y.; Conte, E.; Cao, Y. A Critical Review of Spinel Structured Iron Cobalt Oxides Based Materials for Electrochemical Energy Storage and Conversion. *Energies* **2017**, 10 (11), 1787.

13. Viana, B.; Sharma, S. K.; Gourier, D.; Maldiney, T.; Teston, E.; Scherman, D.; Richard, C. Long term *in vivo* imaging with Cr^{3+} doped spinel nanoparticles exhibiting persistent luminescence. *J. Lumin.* **2016**, 170, 879–887.

14. Zhang, Y.; Wang, J.; Su, Z.; Lu, M.; Liu, S.; Gu, F.; Liu, J.; Tu, Y.; Jiang, T. Spinel $MnFe_2O_4$ nanoparticles (MFO-NPs) for CO_2 cyclic decomposition prepared from ferromanganese ores. *Ceram. Int.* **2020**, 46 (9), 14206–14216.

15. Tabata, M.; Nishida, Y.; Kodama, T.; Mimori, K.; Yoshida, T.; Tamaura, Y. CO_2 decomposition with oxygen-deficient Mn(II) ferrite. *J. Mater. Sci.* **1993**, 28 (4), 971–974.

16. Na, J. G.; Lee, T. D.; Park, S. J. Effects of cation distribution on magnetic properties in cobalt ferrite. *J. Mater. Sci. Lett.* **1993**, 12 (12), 961–962.

17. Playford, H. Y.; Hannon, A. C.; Tucker, M. G.; Lees, M. R.; Walton, R. I. Total neutron scattering investigation of the structure of a cobalt gallium oxide spinel prepared by solvothermal oxidation of gallium metal. *J. Phys. Condens. Matter* **2013**, 25 (45), 454212.

18. Varley, J. B.; Weber, J. R.; Janotti, A.; Van de Walle, C. G. Oxygen vacancies and donor impurities in β-Ga_2O_3. *Appl. Phys. Lett.* **2010**, 97 (14), 142106.

19. Roy, R.; Hill, V. G.; Osborn, E. F. Polymorphism of Ga_2O_3 and the System Ga_2O_3—H_2O. *J. Am. Chem. Soc.* **1952**, 74 (3), 719–722.

20. Playford, H. Y.; Hannon, A. C.; Barney, E. R.; Walton, R. I. Structures of Uncharacterised Polymorphs of Gallium Oxide from Total Neutron Diffraction. *Chem. Eur. J.* **2013**, 19 (8), 2803–2813.

21. Stepanov, S. I.; Nikolaev, V.; Bougrov, V. E.; Romanov, A. Gallium oxide: Properties and Applications – A Review. *Rev. Adv. Mater. Sci.* **2016**, 44, 63–86.

22. Takezawa, K.; Lu, J.; Numako, C.; Takami, S. One-step solvothermal synthesis and growth mechanism of well-crystallized β-Ga_2O_3 nanoparticles in isopropanol. *CrystEngComm* **2021**, 23 (37), 6567–6573.

23. Mendoza-Cachú, D.; Herrero-Calvillo, R.; López-Miranda, J. L.; Esparza, R.; Rosas, G. $FeGa_2O_4$ nanowires preparation after milling and annealing of Fe doped GaN samples. *J. Cryst. Growth* **2019**, 526, 125220.

24. Biswas, S. K.; Sarkar, A.; Pathak, A.; Pramanik, P. Studies on the sensing behaviour of nanocrystalline $CuGa_2O_4$ towards hydrogen, liquefied petroleum gas and ammonia. *Talanta* **2010**, 81 (4-5), 1607–1612.

25. Gurunathan, K.; Baeg, J.-O.; Lee, S. M.; Subramanian, E.; Moon, S.-J.; Kong, K.-j. Visible light active pristine and Fe^{3+} doped $CuGa_2O_4$ spinel photocatalysts for solar hydrogen production. *Int. J. Hydrog. Energy* **2008**, 33 (11), 2646–2652.

26. Omata, T.; Ueda, N.; Hikuma, N.; Ueda, K.; Mizoguchi, H.; Hashimoto, T.; Kawazoe, H. New oxide phase with wide band gap and high electroconductivity $CdGa_2O_4$ spinel. *Appl. Phys. Lett.* **1993**, 62 (5), 499–500.

27. Omata, T.; Ueda, N.; Ueda, K.; Kawazoe, H. New ultraviolet-transport electroconductive oxide, $ZnGa_2O_4$ spinel. *Appl. Phys. Lett.* **1994**, 64 (9), 1077–1078.

28. Can, M. M.; Karaman, T.; Shawuti, S. Optical and structural modification of boron-doped $CoGa_2O_4$ particles. *Ceram. Int.* **2020**, 46 (9), 13025–13032.

29. Chen, H.; Li, G.-D.; Fan, M.; Gao, Q.; Hu, J.; Ao, S.; Wei, C.; Zou, X. Electrospinning preparation of mesoporous spinel gallate (MGa_2O_4; M=Ni, Cu, Co) nanofibers and their M(II) ions-dependent gas sensing properties. *Sens. Actuators B Chem*. **2017**, 240, 689–696.

30. Xu, Z.; Yan, S. C.; Shi, Z.; Yao, Y. F.; Zhou, P.; Wang, H. Y.; Zou, Z. G. Adjusting the Crystallinity of Mesoporous Spinel CoGa2O4 for Efficient Water Oxidation. *ACS Appl. Mater. Interfaces* **2016**, 8 (20), 12887–12893.

31. Liu, D.; Mo, X.; Li, K.; Liu, Y.; Wang, J.; Yang, T. The performance of spinel bulk-like oxygen-deficient $CoGa_2O_4$ as an air-cathode catalyst in microbial fuel cell. *J. Power Sources* **2017**, 359, 355–362.

32. Mohammadi Zardkhoshoui, A.; Hosseiny Davarani, S. S.; Hashemi, M. Fabrication of cobalt gallium oxide with zinc iron oxide on nickel foam for a high-performance asymmetric supercapacitor. *New J. Chem.* **2019**, 43 (11), 4590–4598.

33. Mohammadi Zardkhoshoui, A.; Hosseiny Davarani, S. S.; Ashtiani, M. M.; Sarparast, M. High-Performance Energy Storage Device Based on Triple-Shelled Cobalt Gallium Oxide Hollow Spheres and Graphene Wrapped Copper Iron Disulfide Porous Spheres. *ACS Sustainable Chem. Eng.* **2019**, 7 (8), 7908–7917.

34. Chen, X.; Chai, H.; Cao, Y.; Jia, D.; Liu, A.; Zhou, W. Excellent cycle life of electrode materials based on hierarchical mesoporous $CoGa_2O_4$ microspheres. *Chem. Eng. J.* **2018**, 354, 932–940.

35. He, Z.-H.; Gao, J.-F.; Kong, L.-B. Polycationic bimetallic oxide $CoGa_2O_4$ with spinel structure: dominated pseudocapacitance, dual-energy storage mechanism, and Li-ion hybrid supercapacitor application. *Ionics* **2020**, 26 (3), 1379–1388.

36. Momma, K.; Izumi, F. *VESTA 3* for three-dimensional visualization of crystal, volumetric and morphology data. *J. Appl. Cryst*. **2011**, 44 (6), 1272–1276.

37. Wang, X.; Xu, M.; Liu, L.; Cui, Y.; Geng, H.; Zhao, H.; Liang, B.; Yang, J. Effects specific surface area and oxygen vacancy on the photocatalytic properties of mesoporous F doped SnO_2 nanoparticles prepared by hydrothermal method. *J. Mater. Sci. Mater. Electron.* **2019**, 30 (17), 16110–16123.

38. Kumar, E. R.; Srinivas, C.; Seehra, M. S.; Deepty, M.; Pradeep, I.; Kamzin, A. S.; Mehar, M. V. K.; Mohan, N. K. Particle size dependence of the magnetic, dielectric and gas sensing properties of Co substituted $NiFe_2O_4$ nanoparticles. *Sens. Actuators A Phys*. **2018**, 279, 10–16.

39. Gokul, B.; Matheswaran, P.; Pandian, M.; Arun Paul, C.; Ravikumar, K.; Abd El-Rehim, A. F. Exchange bias and magnetocrystalline anisotropy of non-stoichiometric $Co_xFe_{3-x}O_4$ nanoparticles. *J Mater Sci: Mater Electron* **2022**, 33, 9629–9640.

40. Mathur, S.; Cavelius, C.; Shen, H. $CoGa_2O_4$ Nanoparticles and Films Using a Single Molecular Source. *Z. anorg. allg. chem.* **2009**, 635 (13-14), 2106–2111.

41. Li, J.; Gao, J.-F.; He, Z.-H.; Li, F.-F.; Kong, L.-B. Improving the stable Li^+ storage performance by embedding reduced graphene oxide into cobalt gallium oxide as anode for Li-ion capacitor applications. *Ionics* **2021**, 27 (10), 4153–4165.

42. Taguchi, T.; Ozawa, T.; Yashiro, H. REX2000: yet another XAFS analysis package. *Phys. Scr.* **2005**, 205.

43. Izumi, F.; Momma, K. Three-Dimensional Visualization in Powder Diffraction. *Solid State Phenom.* **2007**, 130, 15–20.

44. Toraya, H. Array-type universal profile function for powder pattern fitting. *J. Appl. Cryst*. **1990**, 23 (6), 485–491.

45. Liu, Z.; Ma, R.; Osada, M.; Takada, K.; Sasaki, T. Selective and Controlled Synthesis of α- and β-Cobalt Hydroxides in Highly Developed Hexagonal Platelets. *J. Am. Chem. Soc.* **2005**, 127 (40), 13869-13874.

46. Melot, B. C.; Page, K.; Seshadri, R.; Stoudenmire, E. M.; Balents, L.; Bergman, D. L.; Proffen, T. Magnetic frustration on the diamond lattice of the *A*-site magnetic spinels $CoAl_{2-x}Ga_xO_4$: The role of lattice expansion and site disorder. *Phys. Rev. B* **2009**, 80 (10), 104420.

47. Ikeda, Y.; Nakayama, N.; Mizota, T.; Nakatsuka, A. Inversion parameter of the $CoGa_2O_4$ spinel determined from single-crystal X-ray data. *Acta Cryst. E* **2006**, 62 (5), i109–i111.

48. Naka, T.; Nakane, T.; Ishii, S.; Nakayama, M.; Ohmura, A.; Ishikawa, F.; de Visser, A.; Abe, H.; Uchikoshi, T. Cluster glass transition and relaxation in the random spinel $CoGa_2O_4$. *Phys. Rev. B* **2021**, 103 (22), 224408.

49. Rafiq, M. A.; Javed, A.; Rasul, M. N.; Nadeem, M.; Iqbal, F.; Hussain, A. Structural, electronic, magnetic and optical properties of AB_2O_4 (A = Ge, Co and B = Ga, Co) spinel oxides. *Mater. Chem. Phys.* **2021**, 257, 123794.

50. Fiorani, D.; Viticoli, S. Magnetic properties of $CoGa_2O_4$. *Solid State Commun.* **1978**, 25 (3), 155–157.

51. Scholl, F.; Binder, K. Selective sublattice dilution in ordered magnetic compounds: A new kind of percolation problem. *Z. Physik B - Condensed Matter* **1980**, 39 (3), 239–247.

52. Mousavand, T.; Naka, T.; Sato, K.; Ohara, S.; Umetsu, M.; Takami, S.; Nakane, T.; Matsushita, A.; Adschiri, T. Crystal size and magnetic field effects in Co_3O_4 antiferromagnetic nanocrystals. *Phys. Rev. B* **2009**, 79 (14), 144411.

53. Kodama, R. H. Magnetic nanoparticles. *J. Magn. Magn. Mater.* **1999**, 200 (1-3), 359–372.

54. Zhang, J.; Naka, T.; Ohara, S.; Kaneko, K.; Trevethan, T.; Shluger, A.; Adschiri, T. Surface ligand assisted valence change in ceria nanocrystals. *Phys. Rev. B* **2011**, 84 (4), 045411.

55. Radha, A. V.; Thomas, G. S.; Kamath, P. V.; Shivakumara, C. Suppression of Spinel Formation to Induce Reversible Thermal Behavior in the Layered Double Hydroxides (LDHs) of Co with Al, Fe, Ga, and In. *J. Phys. Chem. B* **2007**, 111 (13), 3384–3390.

56. Wang, Q.; O'Hare, D. Recent Advances in the Synthesis and Application of Layered Double Hydroxide (LDH) Nanosheets. *Chem. Rev.* **2012**, 112 (7), 4124–4155.

626 57. Cook, D. S.; Wu, Y.; Lienau, K.; Moré, R.; Kashtiban, R. J.; Magdysyuk, O. V.; Patzke,
627 G. R.; Walton, R. I. Time-Resolved Powder X-ray Diffraction of the Solvothermal
628 Crystallization of Cobalt Gallate Spinel Photocatalyst Reveals Transient Layered Double
629 Hydroxides. *Chem. Mater.* **2017**, 29 (12), 5053–5057.

630 58. Hassan, M. R.; Fikry, R. M.; Yakout, S. M. Artificial Neural Network Approach
631 Modeling for Sorption of Cobalt from Aqueous Solution Using Modified Maghemite
632 Nanoparticles. *J. Environ. Eng.* **2020**, 146 (4), 04020013.

633 59. Dakroury, G. A. R.; Abo-Zahra, S. F.; Hassan, H. S.; Ali, H. E. A. Improvement of the
634 sorption behavior of aluminum silicate composite toward ^{134}Cs and ^{60}Co radionuclides by
635 non-living biomass of *Chlorella vulgaris*. *Environ. Sci. Pollut. Res.* **2020**, 27 (17), 21109–21125.

636 60. Sheha, R. R.; Moussa, S. I.; Attia, M. A.; Sadeek, S. A.; Someda, H. H. Development
637 and application of carbon nanotubes reinforced hydroxyapatite composite in separation of Co(II)
638 and Eu(III) ions from aqueous solutions. *Radiochim. Acta* **2018**, 107 (1), 67–82.

639 61. Akagi, T.; Fuwa, K.; Haraguchi, H. Gallium Coprecipitation Associated with
640 Magnesium for Preconcentration of Trace Metals in Seawater. *Bull. Chem. Soc. Jpn.* **1989**, 62
641 (12), 3823–3827.

All graphics for :

Supercritical Hydrothermal Synthesis of Spinel-Type Non-stoichiometric Cobalt Gallate Nanoparticles and Their Magnetic Properties

Bo Xie[a], *Chiya Numako*[b], *Takashi Naka*[c], *Seiichi Takami*[a*]

[a]Department of Materials Process Engineering, Graduate School of Engineering, Nagoya University, Furo-cho, Chikusa-ku, Nagoya 464-8603, Japan

[b]Department of Chemistry, Graduate School of Science, Chiba University, 1-33 Yayoi-cho, Inage-ku, Chiba 263-8522, Japan

[c]National Institute for Materials Science (NIMS), 1-2-1 Sengen, Tsukuba, Ibaraki 305-0047, Japan

13

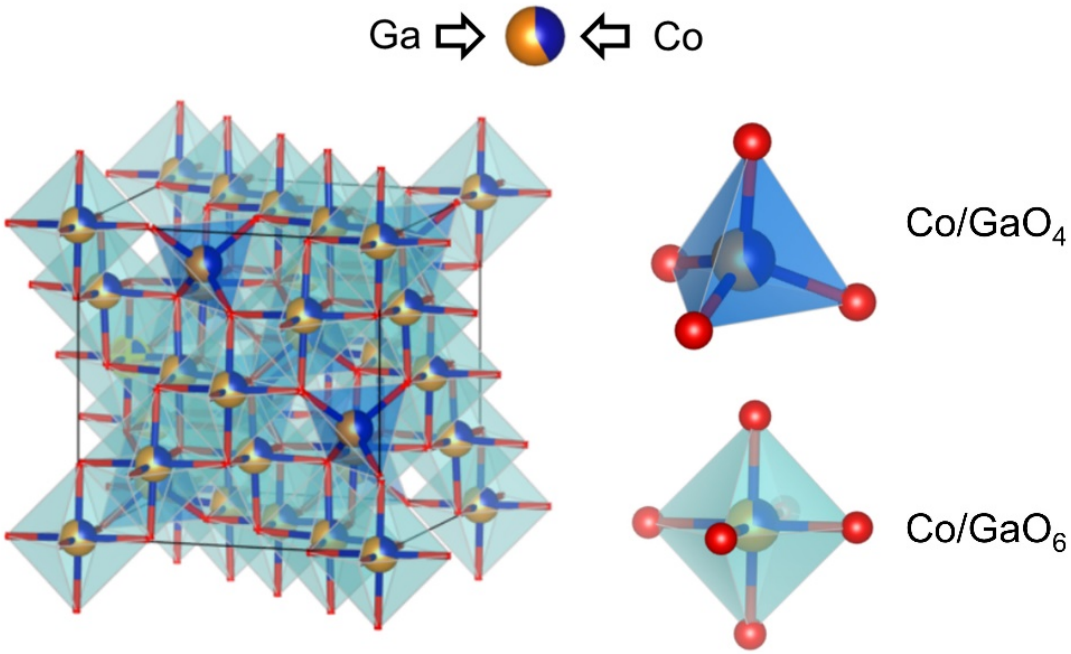

Figure 1. Crystal structure of a partially inverse $CoGa_2O_4$ created by VESTA.

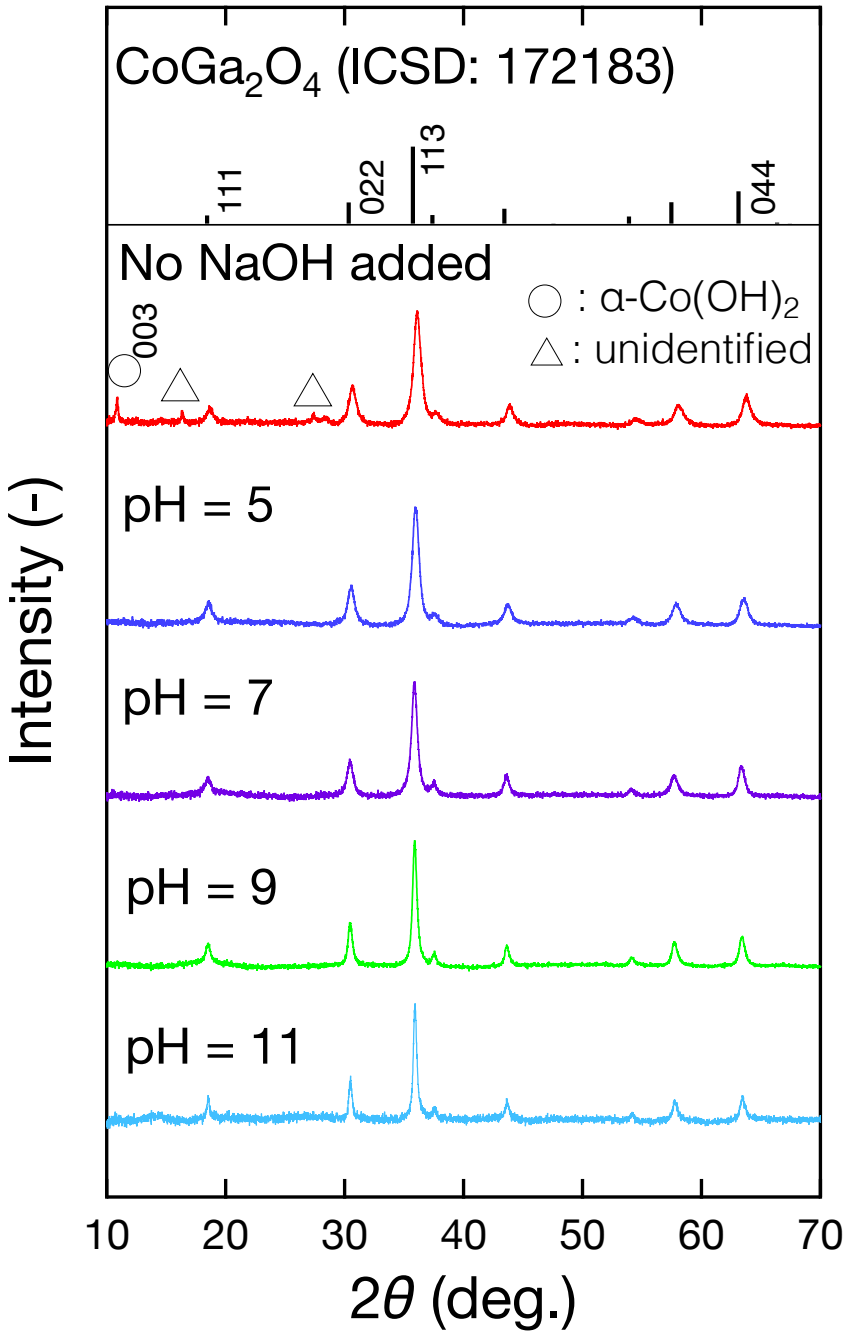

Figure 2. X-ray diffraction patterns of solid products produced at 400 °C under various pH values of precursor solutions.

15

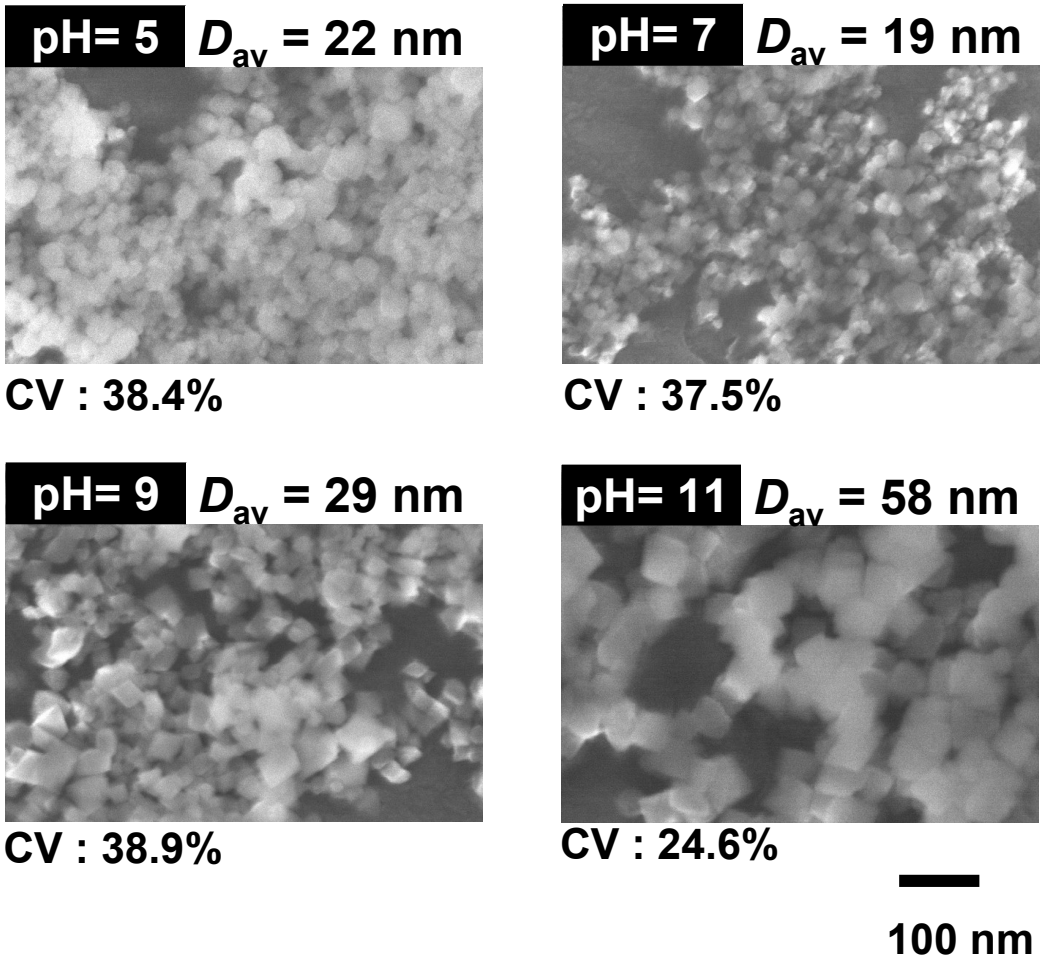

Figure 3. Morphologies and measured average particle sizes of Co–Ga NPs produced at 400 °C under various pH values of precursor solutions (D_{av}: average particle diameter, CV: coefficient of variation).

16

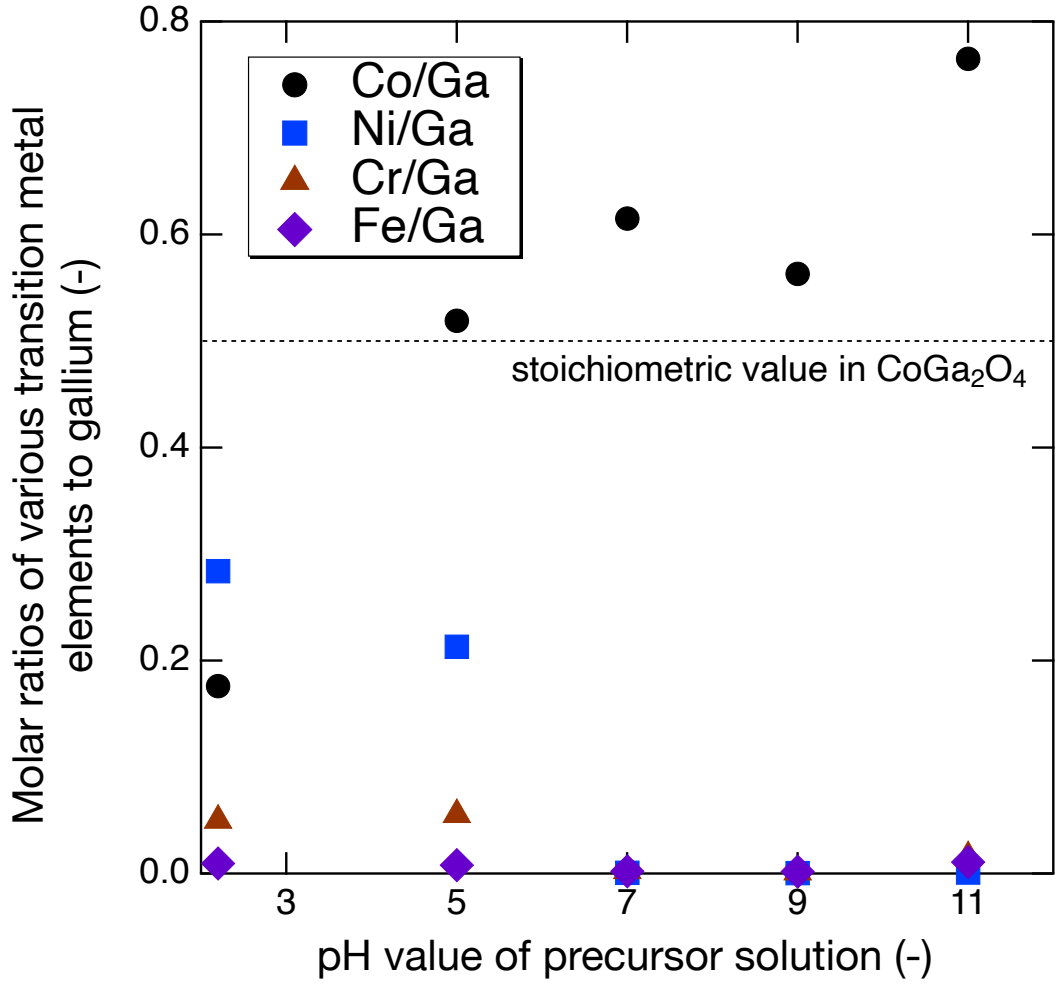

Figure 4. M/Ga (M = Co, Ni, Cr, and Fe) molar ratios of Co–Ga NPs produced at 400 °C under various pH values of precursor solutions measured by ICP-AES.

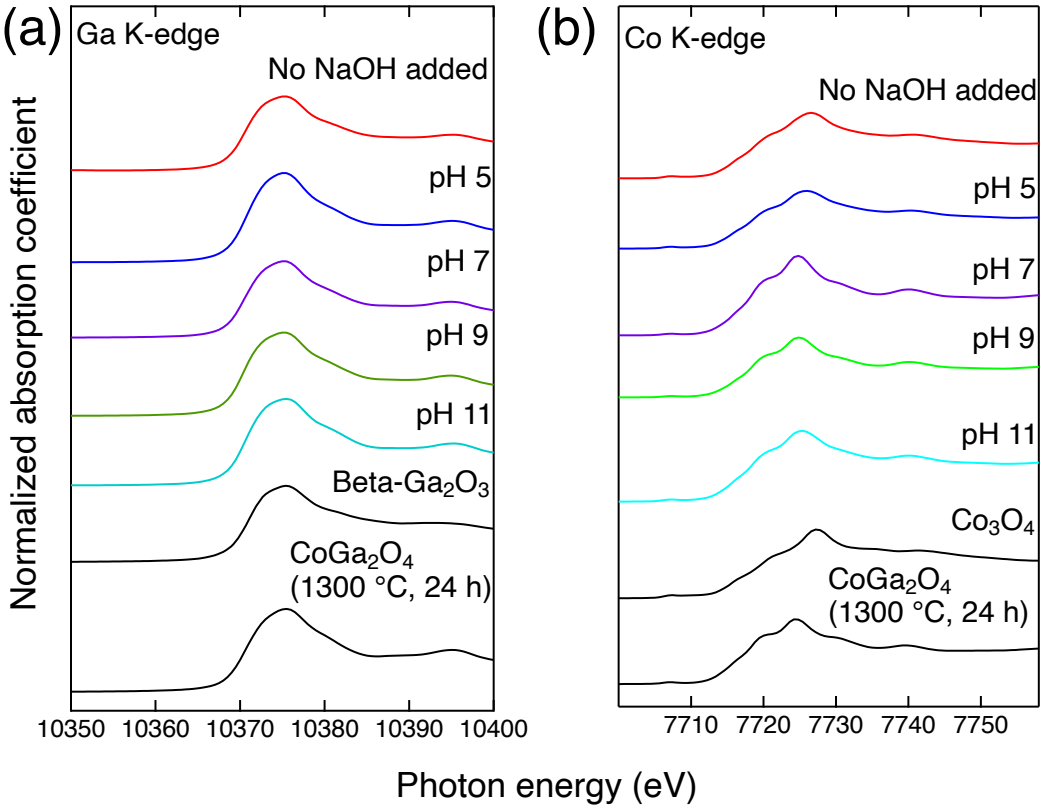

Figure 5. (a) Ga and (b) Co K-edge X-ray absorption near edge structure spectra of non-stoichiometric Co–Ga NPs produced at 400 °C under various pH values of precursor solutions.

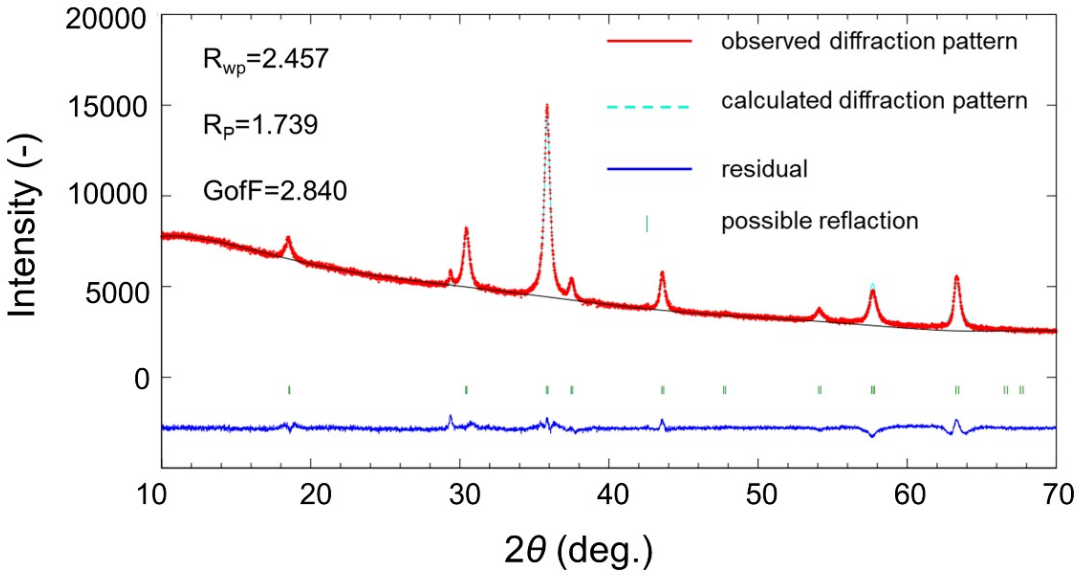

Figure 6. Example (pH 9, 400 °C) of Rietveld refinement using RIETAN-FP in this study.

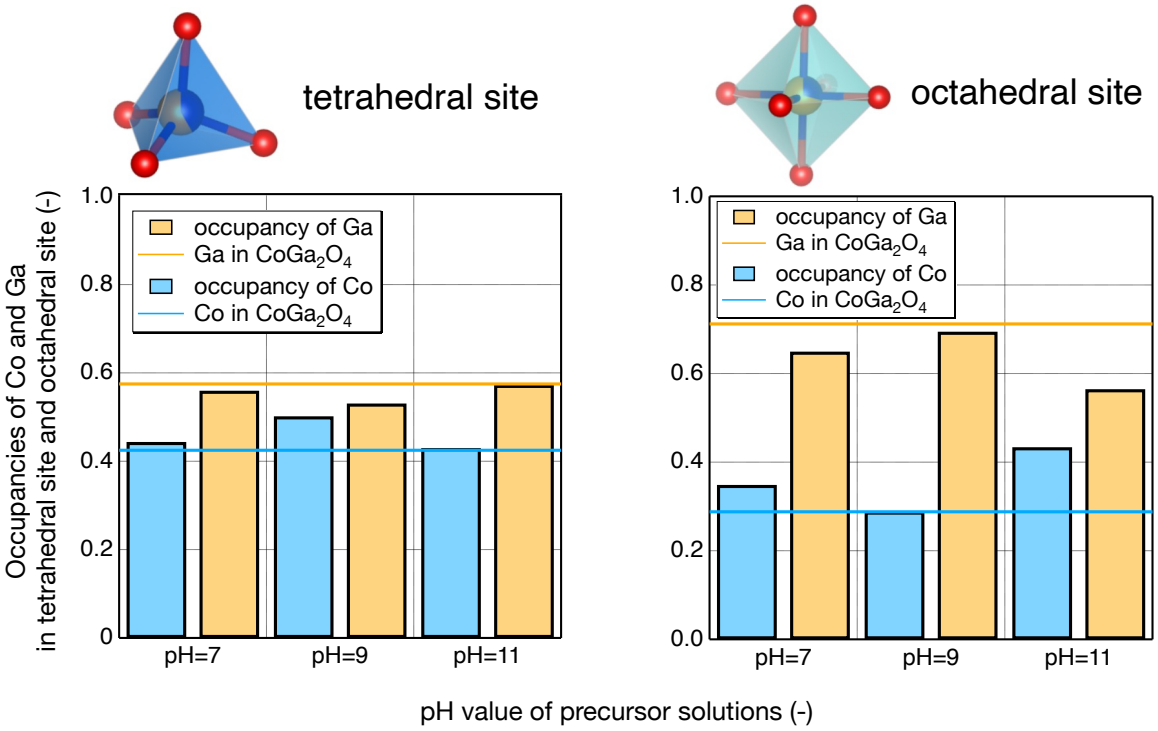

Figure 7. Occupancies of Ga and Co in tetrahedral and octahedral sites derived from Rietveld refinement results of non-stoichiometric Co–Ga NPs produced at 400 °C using precursor solutions with pH 7–11.

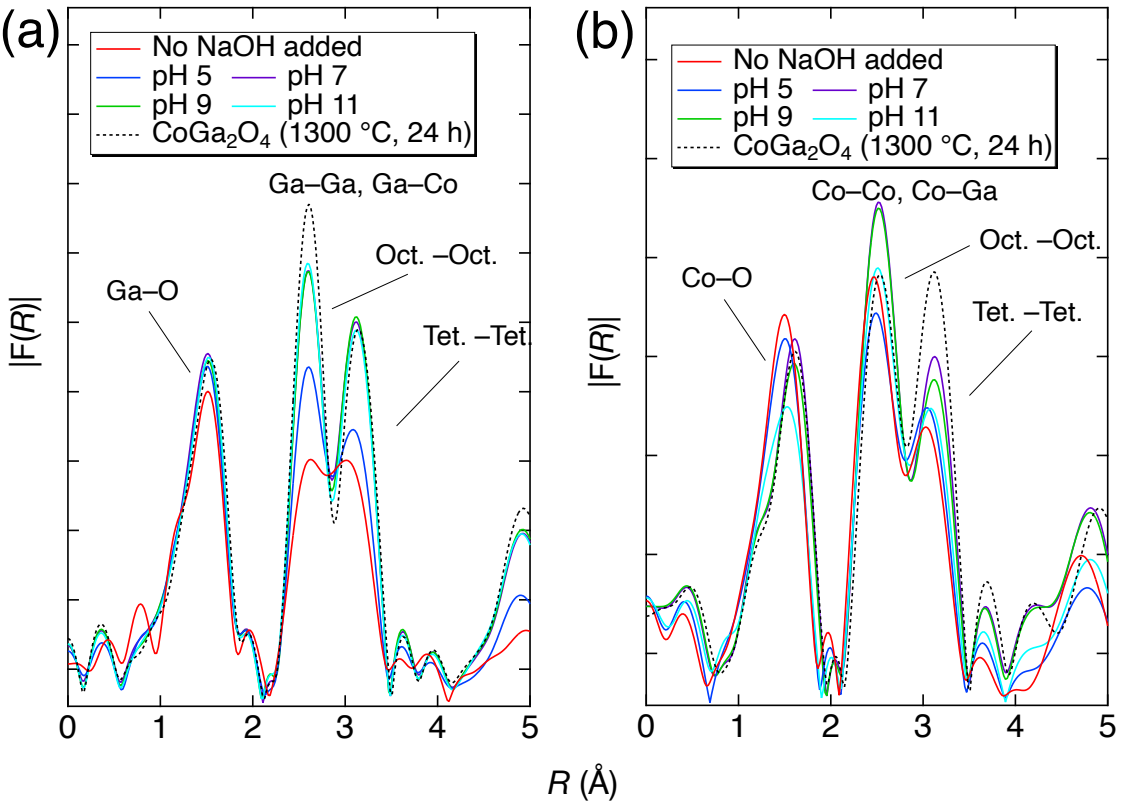

Figure 8. Radial structure function of (a) Ga and (b) Co derived from the extended X-ray absorption fine structure analysis of non-stoichiometric Co–Ga NPs produced at 400 °C under various pH values of precursor solutions.

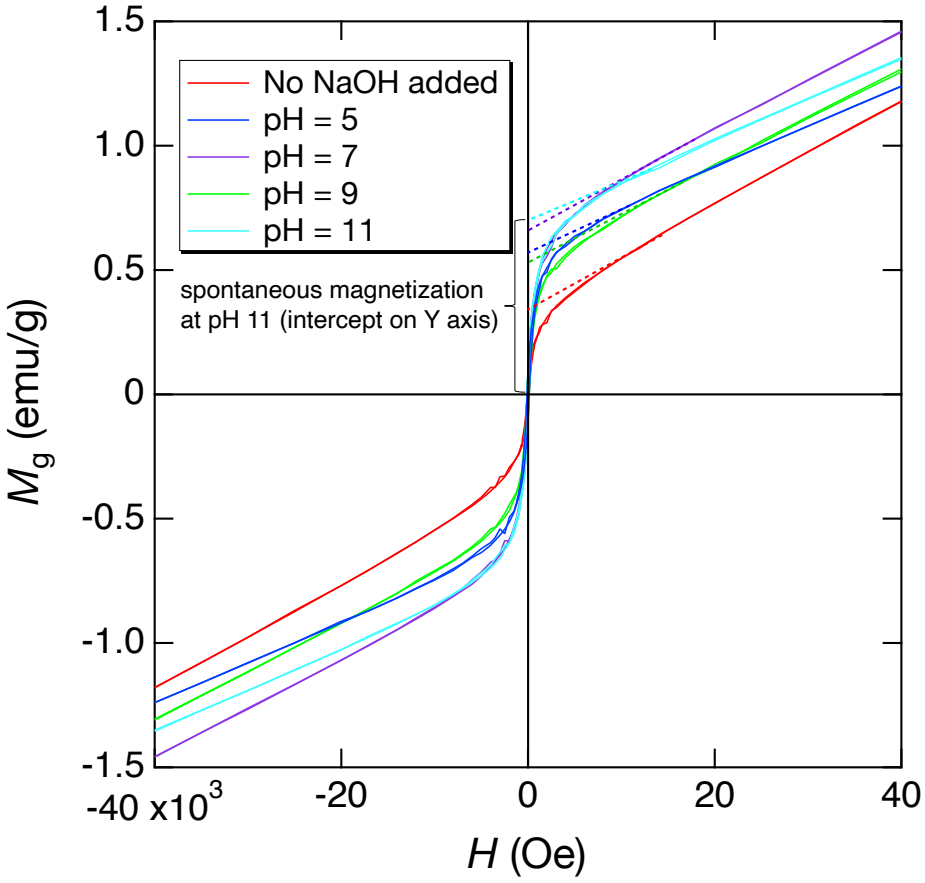

Figure 9. *M–H* curves (measured at room temperature, 300 K) of non-stoichiometric Co–Ga NPs produced at 400 °C under various pH values of precursor solutions.

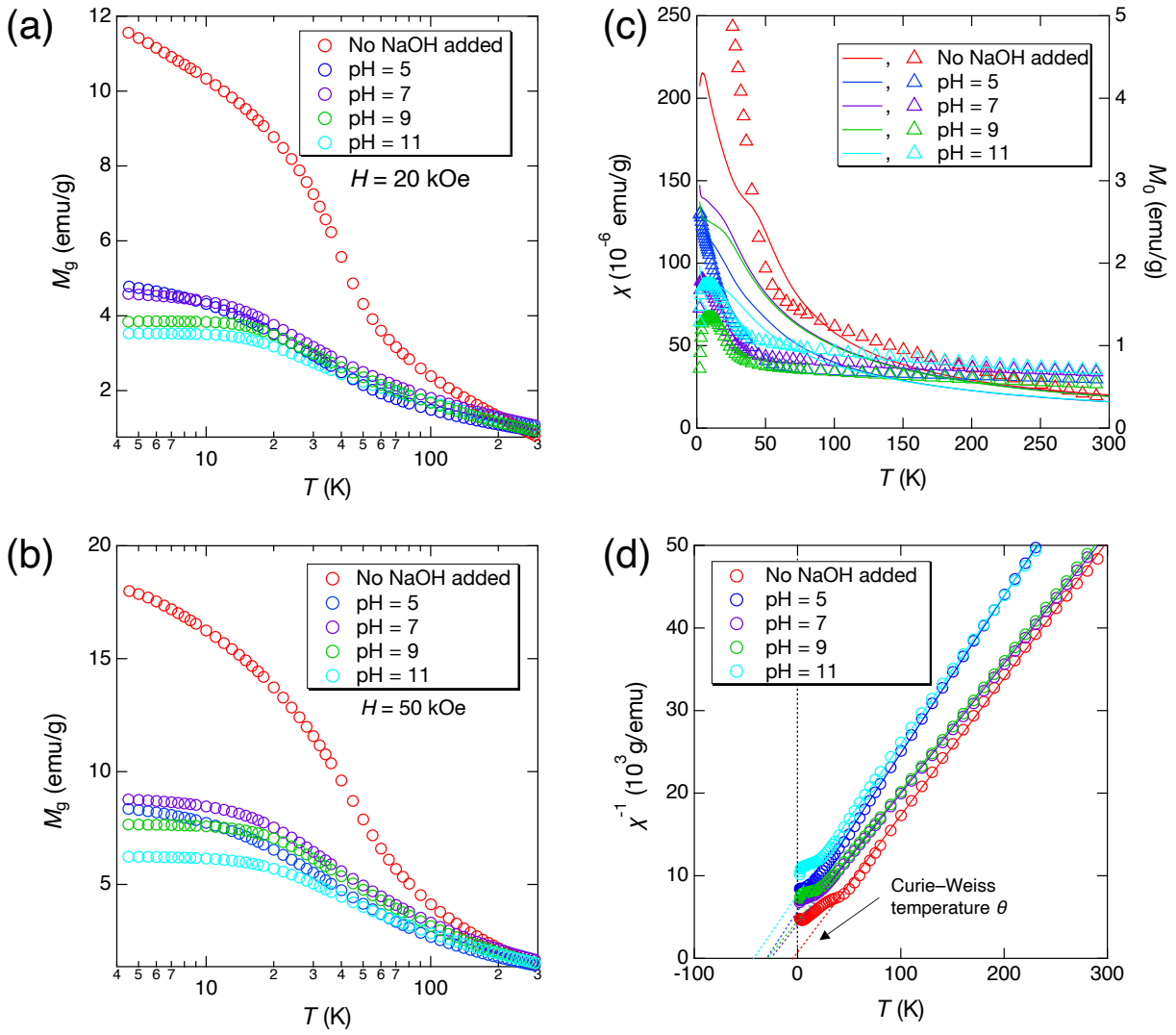

Figure 10. *M–T* curves measured at (a) 20 kOe and (b) 50 kOe and (c) χ, m_0 vs T plots and (d) χ^{-1} vs T plots of non-stoichiometric Co–Ga NPs produced at 400 °C under various pH values of precursor solutions.

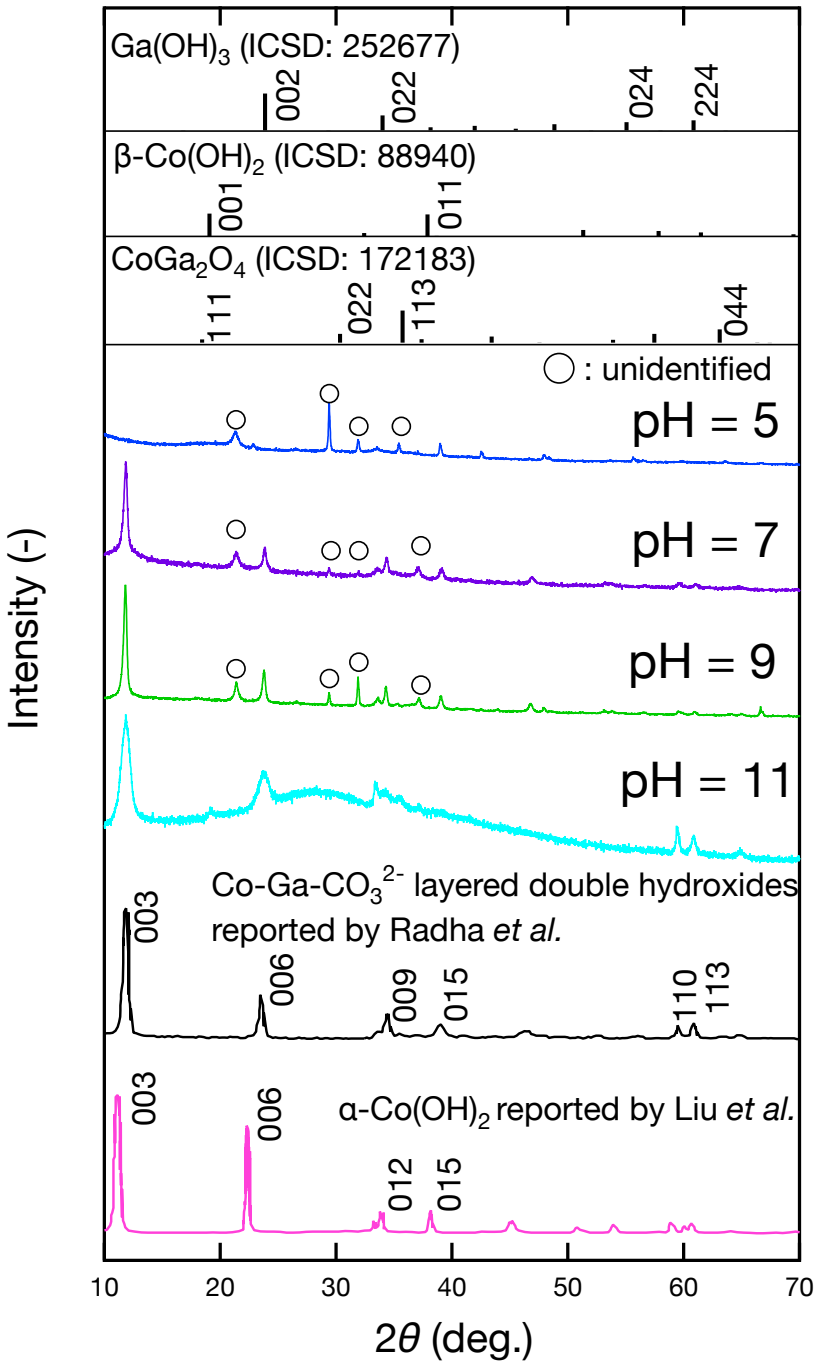

Figure 11. X-ray diffraction (XRD) patterns of solid precipitates in precursor solutions at various pH values. (The XRD patterns of Co–Ga-CO_3^{2-} LDHs and α-Co $(OH)_2$ are plotted based on research papers of Radha *et al.*[55] and Liu *et al.*[45], respectively.)

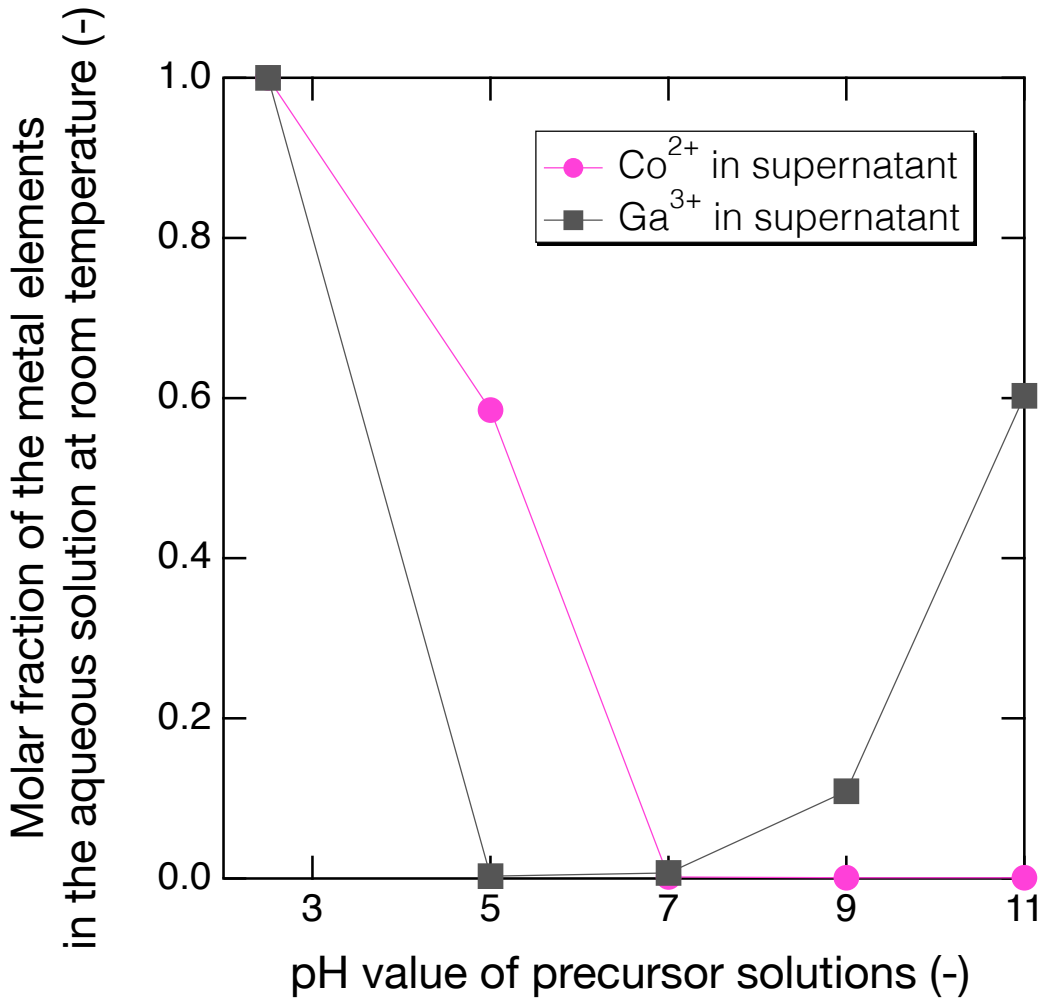

Figure 12. Molar fractions of cobalt and gallium in supernatant of precursor solutions at various pH values.

50

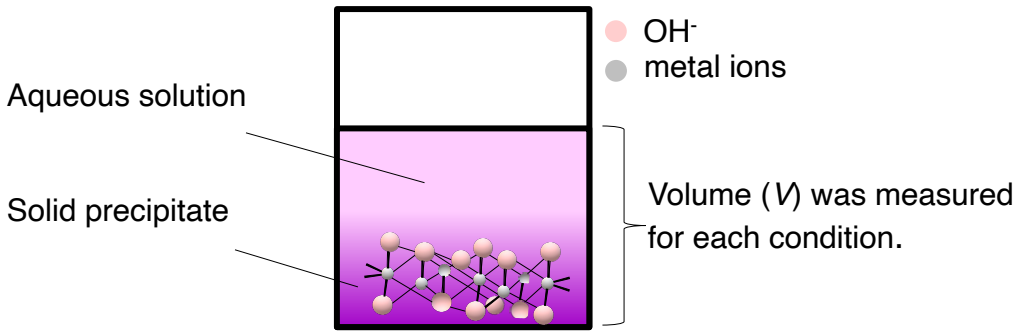

$$M_{(\text{Co, precipitate})} = M_{(\text{Co, in whole precursor solutions})} - C_{(\text{Co, aqusous solution})} \times V$$

$$M_{(\text{Ga, precipitate})} = M_{(\text{Ga, in whole precursor solutions})} - C_{(\text{Ga, aqusous solution})} \times V$$

Figure 13. Schematic depicting the calculation of chemical composition in the solid precipitate.

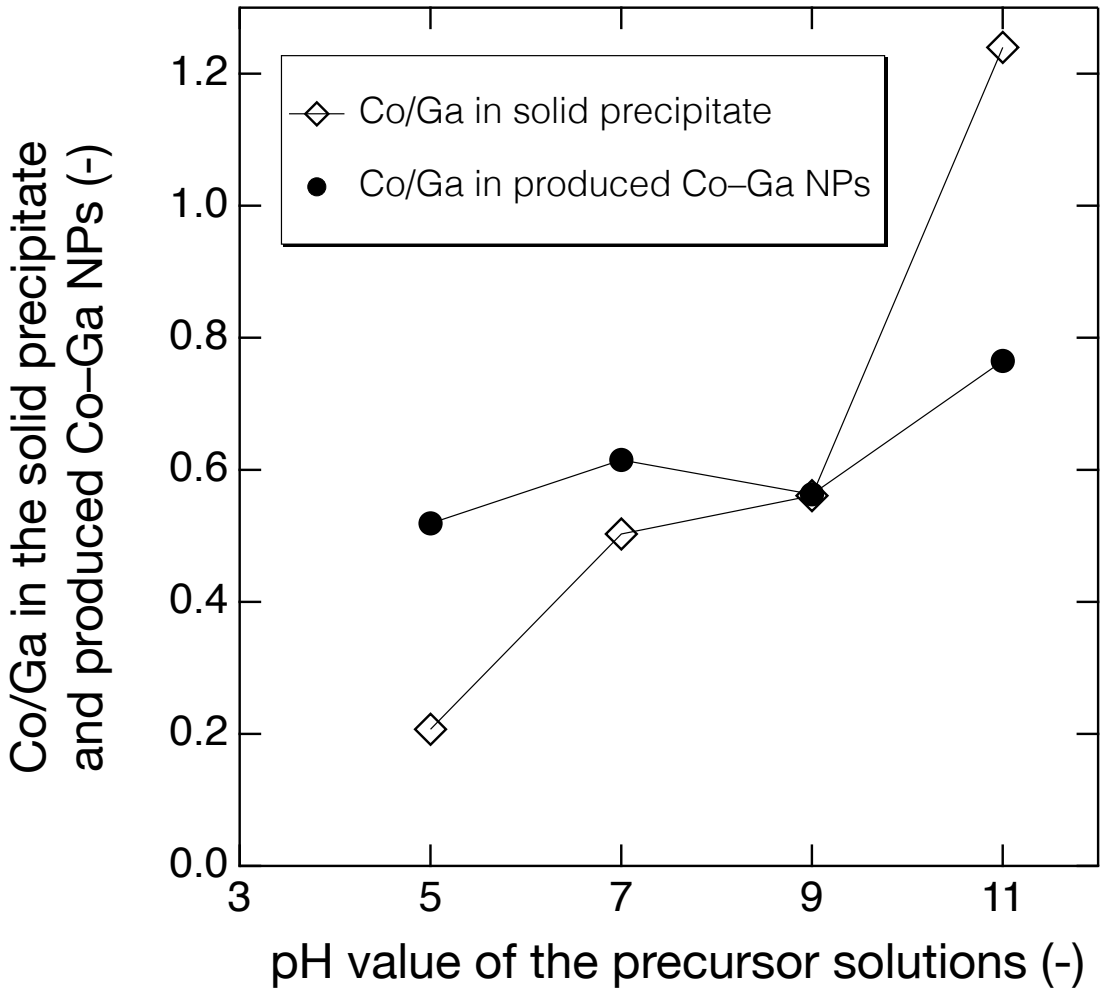

Figure 14. Co/Ga molar ratios in the solid precipitate and produced non-stoichiometric Co–Ga NPs.

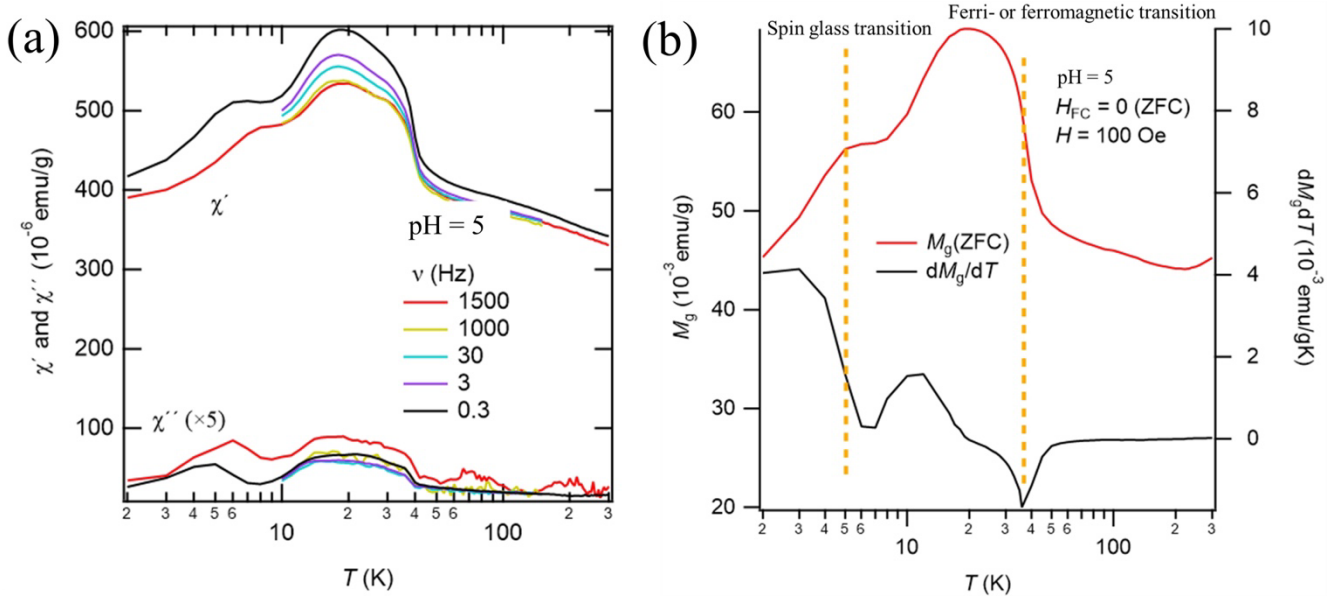

Figure S1. (a) AC susceptibility at various frequencies, (b) DC susceptibility measured after zero-field cooling (ZFC) of the Co-Ga NPs at 400 °C prepared from precursor solutions with pH 5.

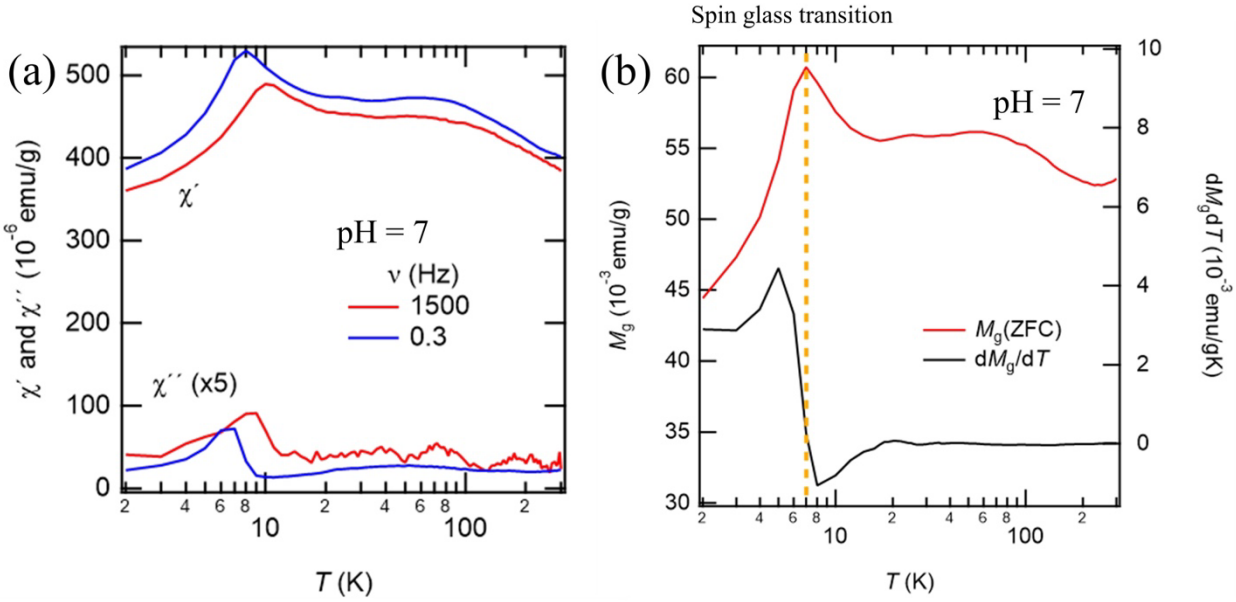

Figure S2. (a) AC susceptibility at various frequencies, (b) DC susceptibility measured after zero-field cooling (ZFC) of the Co-Ga NPs at 400 °C prepared from precursor solutions with pH 7.

62

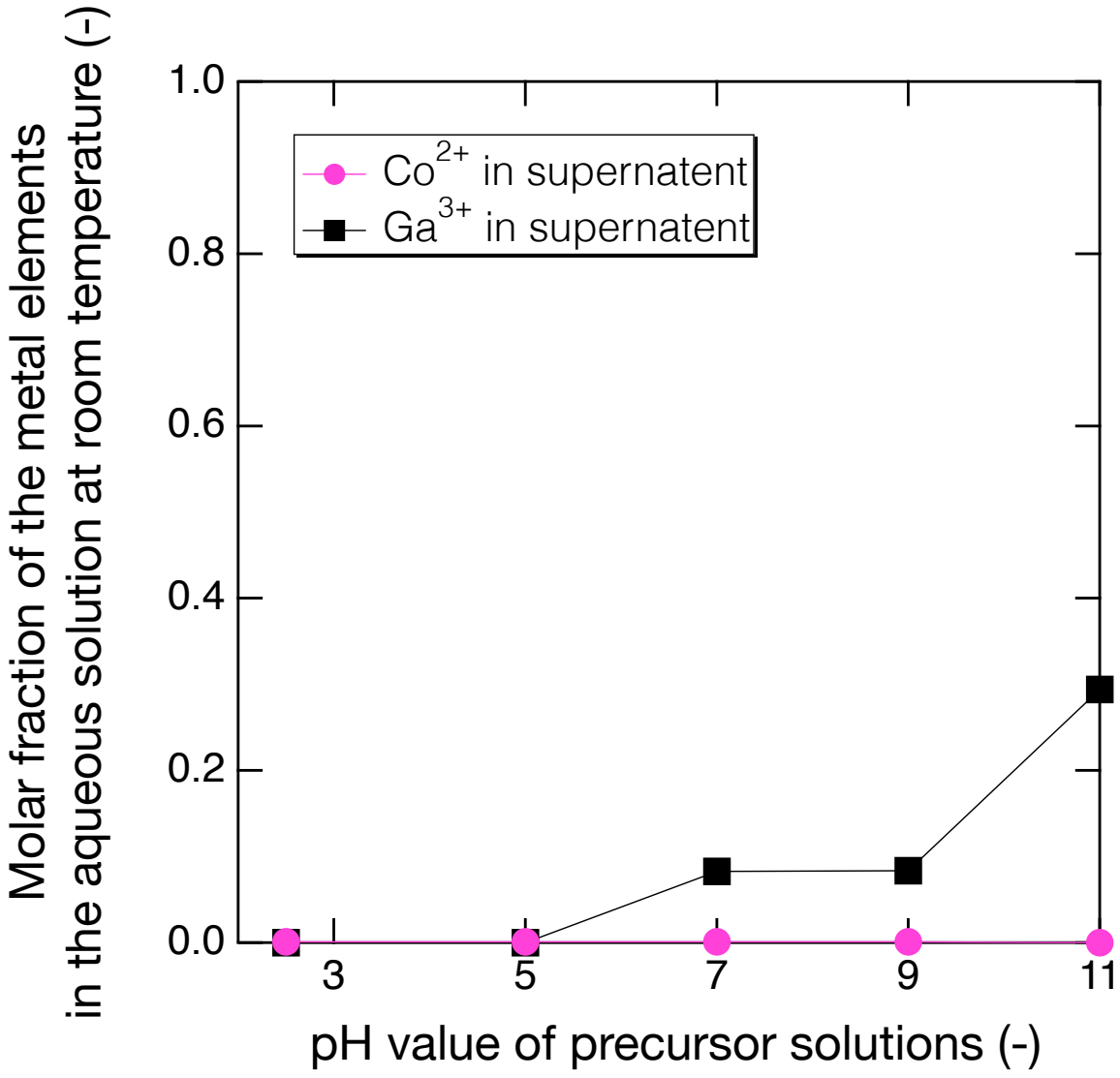

Figure S3. Molar fractions of cobalt and gallium in supernatant of reactant solutions after supercritical hydrothermal synthesis at various pH values..